Throwing light on dark states of organic molecules

Inaugural Dissertation

zur Erlangung des Doktorgrades
der Mathematisch-Naturwissenschaftlichen Fakultät
der Heinrich-Heine-Universität zu Düsseldorf
vorgelegt von
Ferdinand Vogeler
aus Düsseldorf

Düsseldorf, Dezember 2011

Gedruckt mit der Genehmigung der
Mathematisch-Naturwissenschaftlichen Fakultät der
Heinrich-Heine-Universität Düsseldorf
Referent: Prof. Dr. Rainer Weinkauf
1. Korreferent: Prof. Dr. Michael Schmitt
2. Korreferent: Prof. Dr. Ulrich Boesl-von Grafenstein
Tag der mündlichen Prüfung: 25.04.2012

1. Declaration

Hiermit erkläre ich, dass ich die dieser Dissertation zu Grunde liegenden Arbeiten selbstständig und eigenhändig durchgeführt habe. Des weiteren erkläre ich, dass ich diese Arbeit selbständig verfasst und keine anderen als die angegebenen Quellen und Hilfmittel verwendet habe. Etwaige Zitate wurden kenntlich gemacht.

Düsseldorf, Dezember 2011

Ferdinand Vogeler

2. Dedication

Meinen Eltern, meiner Schwester

3. Acknowledgments

Ich bedanke mich herzlichst bei dem gesamten Arbeitskreis:
Prof. Dr. Rainer Weinkauf
Arbeitsgruppe für Lasermassenspektroskopie
Institut für physikalische Chemie I
Heinrich-Heine-Universität Düsseldorf

Besonderer Dank gilt:

Prof. Dr. Rainer Weinkauf der mich nach meiner Diplomarbeit auch als Doktorand stets mit größter Hingabe betreute und durch viele produktive Diskussionen an seinem Wissen im Bereich der physikalischen Chemie teilhaben ließ.

Prof. Dr. Michael Schmitt als Zweitgutachter dieser Arbeit und für seine grandiose Einführung in die Methoden der optischen Spektroskopie.

Dr. Swen Siegert für die Freundschaft in 4 Jahren Diplom- und Doktorarbeit, für die Unterstützung in langen Messnächten und für das gute Teamwork, das großen Anteil am Gelingen des Projektes hatte.

Meinen guten Freunden Janina Hahn und Felix Dollase dafür, dass sie immer ein offenes Ohr für mich hatten.

Nadine Wolters für das gute Klima in unserem Arbeitskreis und die vielen Stunden der konsequenten Hilfe bei der Vorbereitung von Seminaren und Übungen.

Bettina Deckert für den unermüdlichen Einsatz im Umgang mit Universitätsverwaltung und Organisation des Arbeitskreises.

Allen Mitarbeitern des Instituts für physikalische Chemie I der Heinrich-Heine-Universität.

Der Deutschen Forschungsgemeinschaft für die Finanzierung des Sonderforschungsbereichs 663.

Meinen Freunden und Kommilitonen.

Contents

4. Abstract

This work presents current technical innovations and enhancements on a radical anion photodetachment photoelectron spectrometer, with the goal to facilitate an easy experimental method for the location of dark states in organic molecules. Therefore, a high-resolution electrostatic electron spectrometer was constructed and further refined. As the electron spectrometer is the central part of the system, special care was taken to ensure a maximum possible resolution, while still maintaining a long-term manageable setup. Additionally the inlet system was upgraded with a high-temperature nozzle system to allow thermal vaporisation up to 590 K. To prove the benefits of such a system, dark states of different biologically and technically relevant molecules were analyzed. Much of the resulting data has been included in several peer-reviewed publications or will be published shortly.

Die vorliegende Arbeit berichtet über die aktuellen Neuerungen und Verbesserungen an einem Radikalanionen Photodetachment Photoelektronen Spektrometer, mit dem Ziel, eine Methode zur einfachen, experimentellen Untersuchung von dunklen Zuständen in organischen Moleküle zu ermöglichen. Besonderer Wert wurde hierbei auf die Konstruktion eines hochauflösenden elektrostatischen/feld-freien Elektronenspektrometers gelegt, das als zentrales Herzstück des Systems mit seiner spektralen Auflösung über das Gelingen oder Nichtgelingen der Experimente entscheidet. Des Weiteren wurde ein Hochtemperaturdüsensystem entwickelt, das nun die thermische Verdampfung bei bis zu 590 K ermöglicht. Um den Nutzen solcher Experimente darzustellen, wurden Dunkelzustände mehrerer biologisch und technisch relevanter Moleküle vermessen, deren Ergebnisse in diversen Veröffentlichungen wiederzufinden sind.

5. Introduction

Photophysics and photochemistry are important research fields which deal with the photostability of chemical substances, their colors and their optical addressability in industrial applications. A deeper analysis of photochemistry shows that, besides the optically bright states, optically non-visible states exist which, however, can strongly contribute to photophysical and photochemical processes in organic molecules. These states are commonly known as 'forbidden states'. Only a small number of substances of daily life show effects like fluorescence. This admittedly means that most of the molecules absorb light through bright states, but loose the resulting electronic excitation by dark, non-radiative mechanisms. Therefore, the notion of 'forbidden states', which denotes a non-reachable state, seems to be improperly chosen so this work will try to propagate the term 'dark states' for these special electronic transitions. Since, in general, it is assumed that about 50 % of the electronic states in an molecule are dark and mostly unknown, the analysis of the molecule's relaxation mechanisms is usually difficult. As a minimum requirement for reasonable assumptions, the energetic order and relative electronic positions of the electronic states need to be known. Classical optical spectroscopy often fails to obtain values for these special states as the transition moments for allmost all dark states in organic molecules are vanishingly small. Additional problems often arise through the fact that many experiments are being performed in crystals or solution at low temperatures. As enviromental effects can broaden the spectra and shift the resulting peaks these experiments are often inaccurate.

The main goal of this work is to use anion photodetachment photoelectron spectroscopy to have direct access to dark states, such as triplet, nπ^*, charge separated and symmetry forbidden states. The main advantages of radical anion photodetachment photoelectron spectroscopy are, that transitions from the anion should all have similar probabilities and that the anions can be mass-selected before the actual spectroscopy, so exactly one species is analyzed.

The technical enhancements presented in this work include an updated high temperature design of the inlet system and a new high resolution electron spectrometer to be able to measure even tightly spaced electronic transitions. With these improvements dark state spectroscopy was performed on a number of molecules ranging from simple hydrocarbons like aromatic polyenes and azulene, to heterosubstituted biological and technical systems like *p*-benzoquinone, xanthone and its derivatives. As the actual spectra show, it is now possible to perform direct spectroscopy of dark states and the new, improved radical anion photdetachment photoelectron spectrometer is fully functional.

6. Theoretical fundamentals and basic considerations

6.1. Dark state spectroscopy

As mentioned in the introduction, in many organic chromophores, the energetics and role of dark states in photophysics and photochemistry are often discussed controversially in optical spectroscopy. Dark states are molecular electronic states which have a small transition moment in classical, optical spectroscopy of neutral molecules (IR and UV/Vis, for a comparison see chapter 8.2). Starting in S_0, this leads to low intensities in direct absorption spectra and small peaks that are often barely distinguishable from background noise; sometimes if the signal-to-noise-ratio (SNR) is not high enough this even makes these special states completely invisible. Examples of dark states are:

- Triplet states, where two half-occupied electronic levels are populated by unpaired electrons with parallel spins
- $n\pi^*$ states, where the transition takes place between a local non-binding n orbital and a delocalized anti-binding π^* orbital
- Charge-transfer (CT) states, where an electron is transferred from one molecule to another, forming a charge separated state with distinct positive and negative charges on different parts of the resulting molecular cluster. Also intramolecular CT states are possible
- Symmetry forbidden singlet states, and
- Finally, excited states with double excitations in the MO scheme

Nevertheless, many of these electronic transitions are important intermediate states in photochemical and photophysical processes. The energetics of the participating molecules are mostly unknown, so many photophysical or chemically reactive pathways are not quantitatively understood. Dark states, such as triplet states, often play an important role in destructive mechanisms, and should therefore be analyzed in detail. For intermolecular chemistry, many of these mechanisms need special energy storing states with long life-times, to allow diffusion controlled processes and collisional reactions before deactivation. To understand the deactivation processes competing with chemical reactions the Jablonski diagram (Fig. 6.1) is used. In the Jablonski scheme different molecular electronic states (S_0 to S_2, S_n, T_1 and T_2) are shown. Their corresponding vibrational levels are depicted in light gray colors. Once a molecule has absorbed energy ('$h\nu$') in the from of light, shown as a blue arrow for the $S_0 \rightarrow S_2$ transition, a number of different routes back to the neutral ground state are possible. If the system relaxes

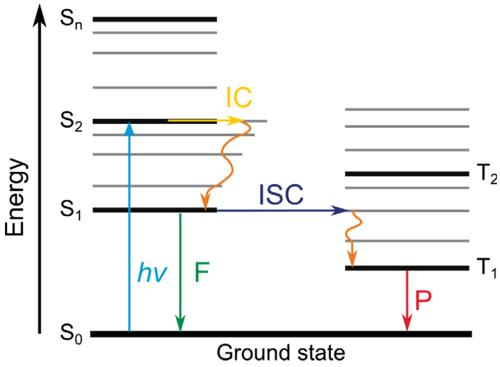

Figure 6.1.: Jablonski diagram. $h\nu$ = photoexcitation, F = fluorescence, IC = internal conversion, ISC = intersystem crossing, P = phosphorescence

radiation-less, the energy conserving process is either called internal conversion (yellow arrow, ‘IC’) or in case of a spin change, intersystem crossing (purple arrow, ‘ISC’). By collision with other molecules the excited vibronic states can now relax into their vibronic ground levels (orange curves). Internal conversion and collisional relaxation from the S_2 normally lead to the lowest excited singlet state S_1. In the singlet pathway, if a photon emission occurs between two states of the same spin multiplicity (green arrow ‘F’, $S_1 \rightarrow S_0$) the emitted radiation is termed fluorescence. Long lifetimes of certain singlet states, in this example the S_1, often favor intersystem crossing processes to triplet states (here: T_1). From the resulting T_1 state it is now possible to return to the ground state by radiative phosphorescence processes (red arrow, ‘P’). Typically, the probability for the radiation-less inter-system crossing process is by many magnitudes smaller and the resulting lifetime accordingly longer than the competing processes, which effectively makes the T_1 state a perfect candidate for energy storage. Lifetimes of different photophysical processes are shown in table 6.1. The Jablonski scheme, despite being a helpful tool to understand photophysical reactions in many molecules, does not cover all possible energetic pathways. For different effects advanced theories have to be considered, including:

Comparison of lifetimes

Relaxation type	Lifetime	Radiation
Fluorescence	10^{-8} to 10^{-10} seconds	Short duration, red-shifted
Phosphorescence	10^{-6} seconds to hours	Short duration, red-shifted
IC $S_2 \rightarrow S_1$	$\leq 10^{-12}$ seconds	none
IC $S_1 \rightarrow S_0$	10^{-9} to 10^{-12} seconds	none

Table 6.1.: Lifetimes of different relaxation processes.

- Conical intersections; two potential energy surfaces of the same spin and spatial symmetry intersect in an energetically degenerated point, creating a 'molecular funnel' where excited states can easily be non-radiatively de-excitated (for an introduction see ref. [BAE06])

- El-Sayed's rule; states that the intersystem crossing rates (a low yield photophysical process involving an isoenergetic radiationless transition between two electronic states of different multiplicities) can significantly be enhanced by involvement of a change in molecular orbital type during the radiation-less transition [ELS63] [LOW66, ELS68]
- Intermolecular processes: charge-transfer states, Dexter's electron transfer [DEX53] and Förster's mechanism for resonant non-radiative energy transfer (FRET)[FOE48]
- Environmental effects; shifts in energetic order and position of the electronic states induced by solvation effects of the surrounding molecules

6.1.1. A short history of dark state spectroscopy

The first mentioning of dark state spectroscopy dates way back to the late 1800s when Sir James Dewar discovered the existence of phosphorescence[DEW80, DEW88a, DEW88b] as the first step towards dark state spectroscopy. It was was not up until 1935, about 50 years later, when A. Jablonski tried a first interpretation of these findings[JAB35]. In 1943 Terenin[TER43, TER44], Lewis and Kasha[LEW44, LEW45] gave the first exhaustive explanation for phosphorescence as a metastable radiative decay of T_1 states to the S_0 ground state.

In these days, experiments were often performed on molecules in solid phase or matrices at very low temperatures. A prominently used matrix was the so called Shpol'skii matrix[SHP63a, SHP63b]. As excitonic and solvation effects of the resulting liquid phase clusters and crystals heavily influence their electronic transitions, other methods had to be investigated for reliable result. By 1972 the first gas phase phosphorescence spectra of naphthalene and pyrene were recorded by van Leeuwen et al.[LEE72]. Prior attempts of measurement had failed due to fast radiation-less relaxation processes competing with the long-lived phosphorescence (0.1 to 10 sec.[LOW66]).

In 1976 Lineberger et al. investigated the T_1 state of NH with photodetachment photoelectron studies on NH^- anions[ENG76]. One year later Smalley et al. introduced the merits of jet-cooled molecular beams in photoelectron studies[SMA77] which were then used by Klots and Compton to produce gas phase anions and clusters by combining jet-cooled molecules and electron attachment[KLO77]. In 1983 Kruit and Read presented the first magnetic bottle photoelectron spectrometer[KRU83] were the detection efficiency of the emitted electron was raised from about 0.03 % to nearly 50 % by introduction of a special magnetic mirror. Eight years after Lineberger, Braumann and his co-workers (1984) showed that it was also possible to measure higher, excited electronic states[DRZ84] of neutral molecules. For this he utilized photodetachment spectroscopy where the photodetachment threshold steps for each neutral state are recorded to give a full spectrum of the electronic states. This setup had the drawback of highly complex measurement equipment where lasers had to be scanned over the range of several electron volts, leading to a high amount of work for the operating scientist. In the meantime Kuppermann et al. had investigated triplet states of ‘polyatomic molecules by low-energy, variable-angle electron impact’[KUP79] spectroscopy (electron energy loss spectroscopy, EELS). In this work a large number small (aromatic) molecules, mostly conjugated polyenes, benzenes, five-membered heterocycles, azo-compounds and different substituted derivatives, were in the focus of investigation. Originally developed by Müller-Dethlefs and Schlag[MUE84a, MUE84b], Neumark et al. applied zero kinetic energy electron (ZEKE) spectroscopy to anions in 1989[KIT89] for structural analysis. High resolution (1.5 up to 0.2 meV) anion ZEKE spectra of FeC_2 and other metal clusters were recorded by Drechsler et al. in 1994[DRE94] to investigate spin orbit energy levels. Later photodetachment photoelectron studies of jet-cooled anthracene and anthracene-water dimers[SCH97] were conducted by Schiedt and Weinkauf. Around the same time Parker et al. developed the velocity-map imaging (VMI) method[EPP97] were the three-dimensional sphere of the ejected electrons is transformed into a two-dimensional image on a spatially resolving microchannel detector. This method was based on the works of Chandler and Saeed[HEL93, HEC95] and relies on the lateral energy of the different kinetic electrons. Further improvements were then accomplished by Neumark et al. with the slow electron velocity-map imaging (SEVI)[OST04] method. Recent studies on higher benzene analogs and clusters were conducted by Tschurl et al.[TSC06a, TSC06b, TSC07]. Table 6.2 gives a short summary about the different dark state spectroscopy studies since the first mentioning of phosphorescence by Dewar in 1880.

6.2. Electronic transitions: Selection rules

As previously addressed dark states are often difficult to energetically locate and assign. Some of the main reasons for small transition moments in photoexcitation are:

- The one-photon-one-electron principle (OPOE)
- Prohibition of spin inversion by photoexcitation

Short history of dark state spectroscopy

Dewar	Phosphorescence	1880
Jablonski	Metastable decay of electronic states	1935
Sklar	First interpretation as triplet states	1937
Lewis, Lipkin, Magel	Triplet triplet absorption	1941
Terenin	Analog.: Spin-forbidden absorptions, atoms	1943/44
Lewis, Kasha	Phosphorescence as $T_1 \rightarrow S_0$ transition	1944
Lewis, Calvin	Phosphorescence/ESR for triplet states	1945
Shpol'skii	Invention of the Shpol'skii matrix	1963
Compton, Christophorou	Electron collision absorption method	1968
van Voorst et al.	Phosphorescence in the gas phase	1972
Lineberger et al.	PD-PES on NH	1976
Kuppermann et al.	EELS on aromatic molecules	1979
Kruit, Read	Magnetic bottle PES	1982
Brauman et al.	Photodetachment spectroscopy	1984
Neumark et al.	ZEKE spectroscopy on anions	1989
Drechsler et al.	High-resolution anion ZEKE spectroscopy	1994
Schiedt, Weinkauf	PD-PES on aromatic molecules	1997
Parker et al.	Velocity-map imaging	1997
Neumark et al.	Slow electron velocity-map imaging	2004
Tschurl et al.	Higher benzene analogs and clusters	2006/07
Siegert	PD-PES: polythiophenes & CT states	2010
Vogeler	PD-PES: nπ* states & polyenes (this work)	2011

Table 6.2.: Updated history of dark state spectroscopy based on [LOW66, MCG69, SIE10].

- Small or vanishing electronic wavefunction overlap
- Electric-dipole-forbidden symmetry (Laporte's symmetry selection rules)

6.2.1. The one-photon-one-electron principle

First postulated by Cederbaum et al. in 1977[CED77] and later confirmed by others in neutral HeI photoionization experiments[ELA84], this principle states that one photon can only interact with one electron. Only states which can be reached by excitation of a single electron are visible in one photon experiments. Figure 6.2 shows that if one electronic state, in this example the S_2, consists of a linear combination of two or more different electron configurations the transition probability may be reduced due to the one-electron-one-photon principle. Here, in configuration b), only one electron has to be moved to reach the left S_2, whereas c) depicts a molecular orbital scheme which shows that the other configuration of the S_2 can only be reached by excitation of two electrons. Note: This one-photon-one-electron selection rule is one of the few restrictions, which also applies to the method used in this work.

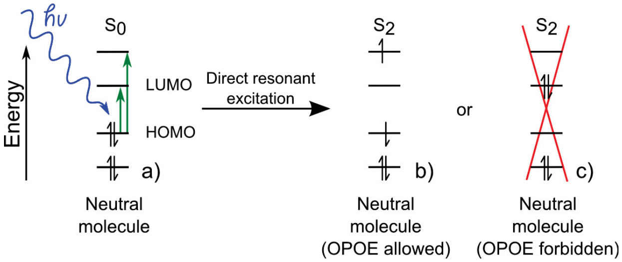

Figure 6.2.: Doubly excited S_2 states in the MO scheme. a) Ground and b), c) excited state configurations. Only state b) is reachable by direct photoexcitation as state state c) differs by two electron positions, which is not allowed by the OPOE selection rule.

6.2.2. Prohibition of spin inversion by photons

In electronic transitions the transition dipole operator describes the interaction of the electric wave of the light with the molecule. In contrast, the electronic spin is a magnetic property. In this context singlet state ($s = 0$) describes an electronic state where all electron spins are compensated, whereas in triplet states ($s = \pm\frac{1}{2}$) two electron spins are aligned in parallel. When exciting an electron with a photon from state 1 to state 2 the integral over the wavefunctions and the dipole operator is obviously not zero. This requirement can be expressed with the formula:

$$P = \left|\langle \varphi_2^* \left|\widehat{\mu}\right| \varphi_1 \rangle\right|^2 = \left| \int_{-\infty}^{+\infty} \varphi_2^* \widehat{\mu} \varphi_1 d\tau \right|^2 \tag{6.1}$$

Where P is the probability amplitude, $\widehat{\mu}$ is the transition dipole operator and respectively φ_2^* & φ_1 are the overall wavefunctions for the final and the initial state. In this concept a magnetic transition is not included. The coupling between singlet and triplet states is weak and only induced by the spin-orbit operator. Figure 6.3 shows how Equation 6.1 transforms into the molecular orbital state scheme. A laser pulse (hν) excites one electron into a higher molecular state. If the overall spin S (sum of all spins s) is not allowed to change, the molecule stays either in the singlet or triplet configuration (Fig. 6.3). Photoinduced transitions from the S_0 to a triplet state (shown here: T_1) are therefore not possible without a spin change. As spin functions are orthogonal, a transition between different spin functions would lead to a transition moment of zero, i.e., this transition would have a low intensity. In molecules with

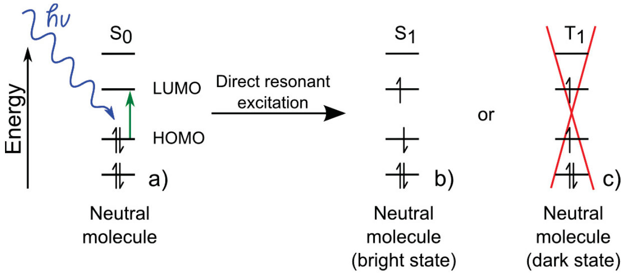

Figure 6.3.: Transitions to the singlet and triplet states, S_1 and T_1 in a MO scheme. Singlet-singlet transition are electric dipole allowed, singlet-triplet transitions are electric dipole forbidden due to prohibition of spin inversion.

heavy atoms (high number of electrons present), the $L - S$ coupling turns into a $j - j$ coupling and the S-T transitions gain intensity with increasing atomic size (e.g., in I_2, CH_3I). Other, additional pathways to population of triplet states are possible; the most prominent being the non-radiative inter-system crossing (ISC) process. From an excited singlet state ISC isoenergeticaly converts population from the singlet to the triplet configuration by spin flipping. The resulting vibrationally excited triplet state then relaxes back into its vibrational ground state.

6.2.3. Small wavefunction overlap

As noted above the transition moment is given by $\mathrm{M} = \langle \varphi_2^* \left| \widehat{\mu} \right| \varphi_1 \rangle$. Since the operator $\widehat{\mu}$ does not shift wavefunctions, φ_2^* and φ_1 must have at least some spatial overlap. For nπ^* transitions an electron is transferred from an localized n orbital to a delocalized π^* orbital. Often, only a small spatial overlap exists between these two orbitals especially if perpendicularly oriented. Therefore, the nπ^* transitions are weak in classic optical spectra. This also applies to charge-transfer (CT) states (intra- as well as intermolecular), where an electron is transferred between two molecules or one localized π system to another within the same molecule. In intermolecular CT transition the problem of non- or only minimally overlapping wavefunctions is even worse than in nπ excitations. The participating wavefunctions are not only separated by mere two or three C-C bonds (about 150 pm each) but by the free space between the involved molecules. Therefore even if the transition is spin and symmetry allowed the resulting transition probability is rather low due to the lack of wavefunction overlap.

6.2.4. Electric-dipole-forbidden transitions (Laporte symmetry selection rules)

The Laporte rule, named after Otto Laporte[LAP25], states that only those electronic transition are allowed where the symmetry or asymmetry in respect of an symmetry center is not conserved. This means that, if the initial state has a g (gerade) symmetry the final state has to be u (ungerade) and if the initial state has an u (ungerade) symmetry the final state has to be of g symmetry (In short: in a transition $\widehat{\mu}$ has a u symmetry and $\langle \varphi_j^* | \widehat{\mu} | \varphi_i \rangle$ should always be of g (gerade) symmetry to be allowed). States denominated as g/u are asymmetric/symmetric in respect of their center of symmetry. If all atoms are inverted across the molecule's inversion center, the relevant molecular property, here the electronic wavefunction, would either look exactly the same (g symmetry) or not (u symmetry). Special effects, like Renner-Herzberg-Teller couplings[HER33, REN34], can soften these rules (also see: Jahn-Teller effect[TEL37]). If an asymmetric vibration deforms the involved molecules they are no longer perfectly symmetric. Since the electrons follow the nuclei the electronic wavefunction becomes an asymmetric contribution, which allows it to couple to a nearby allowed state of this symmetry. As Laportes rule only applies to molecules with a inversion center the imposed rules no longer effects the transition probability. The intensity given by the Renner-Herzberg-Teller couplings, however, are small in comparison to allowed transitions.

6.3. Mass spectrometry

In most spectroscopic methods it is inevitable that only a single type of molecules is present in the analyzed sample volume. For example, carotenes are well known to form aggregates even in small concentrations. As no way of chemical discrimination is known, a physical selection has to be conducted. In gas phase experiments, with their naturally low molecule density, often fragmentation occurs during vaporisation and clustering or dissociation after electron attachment forms new species. Therefore, for some spectroscopic methods, mass selection has to be performed prior to spectroscopy to obtain a direct correlation between molecular species and the optical spectrum and effectively eliminate overlapping subspectra. This also gives the opportunity to investigate stepwise complexation with an increasing number of solvent molecules to understand solvation or delocalization effects in detail. Many different developments were made since the early 1900s, when the first mass analyzers were invented. Table 6.3 gives a short overview about the different types of mass selection methods. This work mainly relies on time-of-flight mass spectrometry (TOF-MS) in combination with mass gating for mass separation.

Method	**Remarks**
Magnetic sector field mass analyzer	Scanning system, low transmission, bulky
Time-of-flight mass spectrometer	High transmission, low resolution, low cost
Electrostatic mass gating	low-/high-pass possible, needs 2nd mass gate
Quadrupole mass filter	Scanning technique, very-low transmission
Quadrupole ion trap	See quadrup., Add. long measurement cycles
Fourier-transform ion cyclotron spec.	Very expensive system, high resolution
Orbitrap	Expensive electronics & mechanical system

Table 6.3.: Different types of mass selectors

6.3.1. Time-of-flight mass separation

The process of mass selection is performed by isolation of different mass-to-charge ratios in the mass spectrometer. Each mass selection method therefore has its advantages and disadvantages. For anion PD-PES, one advantage is the possibility of mass separation before the actual spectroscopy. A TOF-MS system was chosen because of its:

- High transmission of about 50 percent, so that spectra can be obtained despite a very low number of anions
- Theoretically unlimited mass range
- Simple non-scanning system: detection of a full mass spectrum for each measurement cycle
- No high frequency (RF) electronic or magnetic fields disturbs the electron spectrometer
- Compatibility with pulsed sample injection and laser systems
- Low cost in comparison to other types of mass analyzers
- Easily scalable system: cheap ion reflectors and mass gates for higher mass resolution

The ideal starting condition for a time-of-flight mass spectrometer is an ion cloud where the different masses start in one point with zero velocities. This directly translates into identical kinetic energies after acceleration in the ion source. For a given set of masses m$_i$, their velocities can then be written as:

$$E = m_i v^2 \Leftrightarrow v = \sqrt{\frac{2E}{m_i}} \tag{6.2}$$

Where E is the kinetic Energy, m the mass and v is the velocity of the molecules

If multiple charged ions are possible it is necessary to consider that:

$$E = zeU \tag{6.3}$$

Where E is the kinetic Energy, z the charge number, e the charge and U the potential difference of the accelerating electrostatic field.

Combination and transformation of equation 6.2 and 6.3 then leads to equation 6.4 for the velocity of the ions in the field-free flight path.

$$v = \sqrt{\frac{2E}{m_i}} = \sqrt{\frac{2zeU}{m_i}} \tag{6.4}$$

Rewriting the velocity as fractions of distance per time unit directly shows that time-of-flight MS only measures a mass-to-charge ratio:

$$\frac{m_i}{ze} = \frac{2U}{x^2} t^2 \tag{6.5}$$

$\frac{m}{ze}$ = mass-to-charge ratio, U = acceleration potential, x = distance and t = time step.

Note that in equ. 6.3.1 the amount of time during acceleration is not considered. So if the charge numbers z of the analyzed molecules are known, it is possible to calculate their respective masses. As for our ionization method z is always $= -1$, $\frac{m_i}{ze}$ can be represented as m_i. As all spectrometers have to be calibrated on first use, the resulting $\frac{m_i}{ze}$ have to be callibrated against known masses. To predict the ion's arrival times equation 6.3.1 needs further refinement. Equation 6.6 additionally compensates for the acceleration field in the ion source[BOT00].

$$t = \sqrt{\frac{2m_i d}{zeE_{field}}} + L\sqrt{\frac{m_i}{2zeU}} \tag{6.6}$$

m = mass of particle, z = charge number, e = electronic charge, E_{field} = electrostatic field applied in source, d = length of accelerating path, L = length of field-free region and U = accelerating potential

The first term of equation 6.6 handles the problem of starting positions (different d$_i$) in the ion source. The second one describes the field-free drift region of the mass spectrometer. The principle of mass spectrometry dates back to the works of J.J. Thomson in the late 1800s[THO97, THO13]. Despite numerous works in 1913-1940s where different approaches were applied (Research by Arthur J. Dempster[DEM18] resulting in the 1935s discovery of ^{235}U), the first proposal for a fully functional time-of-flight mass spectrometer was made by Stephens in 1946[STE46]. Later revisions by Wiley et al. incorporated a first-order ($\frac{dt}{dx} = 0$)[WIL55] correction for different starting positions of the ions. Further correction of the starting position's effects were achieved by the development of the ion reflector by Marmyrin et al.[MAM73]. Weinkauf et al. then upgraded Wiley's ion source layout with two acceleration fields and highly optimized spacing between the three plates in 1989[WEI89, BOE92] to achieve a second-order corrected temporal focus. To calculate the required distances and potentials equations 6.7 through 6.9[WEI89] can be used.

Distance between ionization site and attracting plate:

$$a = \frac{c-2b}{2(c+b)} \left(c \left(\frac{c-2b}{3c} \right)^{3/2} + b \right) \tag{6.7}$$

a = distance between ionization site and second plate, b = distance between second and third plate, c = distance between third plate and spatial focus

Potential at the second plate:

$$U_{p2} = U_{tot} \left(\frac{2c+2b}{3c} \right) \tag{6.8}$$

U$_{p2}$ = potential at the second plate, U$_{tot}$ = total acceleration potential

Potential at the first plate (repeller):

$$U_{rep} = U_{tot}\left(\frac{2c+2b}{3c} + \frac{x}{a} * \frac{c-2b}{3c}\right) \tag{6.9}$$

U_{rep} = potential at the repeller plate, U_{tot} = total acceleration potential

The addition of two more acceleration plates providing the ion cloud with another spatial focus for further improvement of transmission efficiency. For resolution enhancement different other methods were developed: the already mentioned reflectron TOF-MS[MAM73], velocity compression[MUG87], impulse-field focussing[BRO81] and post-source pulse focussing[KIN89]. To refine temporal, spatial and energetic focusing in this work a variable impulse-field ion source was used[VOG09, SIE10].

6.4. Electron spectroscopy

In this work electron removal with laser radiation is used to perform spectroscopy of dark states by starting in the radical anion. This process of electron removal is called photodetachment.

6.4.1. Electron detachment

Photodetachment describes the effect of removing electrons from anions through photoinduced excitation of the molecules over the detachment threshold. This process is similar to photoionization of neutral gases and surfaces and obeys the same rules except the threshold behaviour. To understand the basics of photodetachment, the photoelectric effect, as discovered in metal surfaces, has to be referred to. First hypothesized by Planck in the year 1900 (quantization of light[PLA00]) the Hallwachs-effect (H. Hertz, W. Hallwachs 1886/87) serves as the basis of photodetachment spectroscopy. Until quantum-physically explained by Einstein in 1905[EIN05] (Nobel prize in physics 1921), it was unclear whether the ejection of electrons only depended on the wavelength of the incident light or also on its intensity. The new assumption was, that light consisted of discrete energy packets (termed 'photons') with their energy ($h\nu$) governed by the radiation's wavelength ($\lambda = \frac{c}{\nu}$). Photons striking matter would then cause the ejection of electrons in one-to-one processes. For metal surfaces, the relation between the energy of the ejected electrons and the energy of the incident photons can be expressed as:

$$E_{kin,e^-} \leq h\nu - \Phi \tag{6.10}$$

Where E_{kin,e^-} is the kinetic energy of the emitted electrons, $h\nu$ is the wavelength and Φ is the work function of the metal surface

Note that due to the band character of the electronic states in metals, with increasing energies also electrons from lower electronic states are ionized so that a part of the photon's energy remains in the atoms. The work function Φ can be presented as the minimum binding energy $\Delta E_{neutral,ion}$ of the electron in the surface. This concept was later transferred to molecules by D.W. Turner[TUR70]. For molecular systems, equation 6.10 can be rewritten as[ATK97]:

$$E_{kin,e^-} = h\nu - \Delta E_{neutral,ion} \tag{6.11}$$

In 1934, Tjalling Koopmans found that during the process of ionization the electronic structure of molecules does not change, so that the energy to remove an electron from a specified atomic or molecular orbital is always constant. This energy was termed one-electron energy ϵ_r. He further stated that the corresponding ionization energy (IE) is directly equivalent to the negated value of the one-electron energy[KOO34, ATK97].

$$IE = -\epsilon_{r,i} \tag{6.12}$$

This method allows determination of $\epsilon_{r,i}$ and additionally cation excited states. If an anion is subjected to photoionisation (termed: 'photodetachment'), the energetic difference between the anion and the neutral ground state is called electron affinity (EA = - $\epsilon_{r,i}$). Since electrons can also be removed from deeper orbitals, photoelectron spectroscopy also gives information on the excited states of the ions. In radical anions this is a valuable addition to the obtained data.

6.4.2. Photodetachment photoelectron spectroscopy

With the text book knowledge of the photoeffect and Koopmans' theorem the principle of PD-PES can be explained. The kinetic energy of the emitted electrons is given by equation 6.11:

$$E_{kin,e^-} = h\nu - E_{Be} \tag{6.13}$$

E_{kin,e^-} = kinetic energy, h = Plancks constant, ν = light waves frequency, E_{Be} = electron binding energy

With the classical physics definition of kinetic energy $E_{kin} = \frac{1}{2}mv^2$ the electron's kinetic energy can be expressed as a function of the electrons mass and velocity:

$$E_{kin} = \frac{1}{2}m_e v_e^2 = h\nu - E_{Be} \tag{6.14}$$

m_e = mass of the electron, v_e = velocity of the electron , $h\nu$ = energy of the photon, E_{Be} = electron binding energy

The equation can then be solved for E_{Be}, so that the velocity can now be translated into the binding energy of the electron in the molecule[KEN92]. In radical anion photo detachment photo electron spectroscopy a laser pulse detaches electrons from open-shell anions. Neutrals are thereby formed and the resulting kinetic energy of the electrons is measured by time-of-flight energy spectrometry. Equation 6.15 describes this in an abstract manner.

$$A(v_0)^- + h\nu \rightarrow N(v_n) + e^-_{kinetic} \tag{6.15}$$

$A(v_0)^-$ = anion in vibronic ground state, $N(v_n)$ = neutral in any reachable vibronic state, $e^-_{kinetic}$ = emitted electron

The equation also shows that it is possible to reach many final vibronic states so electronic, vibrational and rotational information should be contained in the resulting data. Figure 6.4 explains this process in an electronic state scheme. The molecules are ionized into radical anions by attachment of an electron from the neutral ground state (shown as

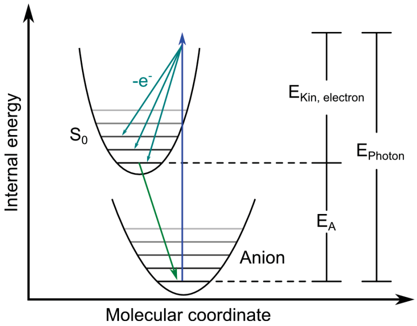

Figure 6.4.: Electron detachment and electron affinity in PD-PES. Only $D_0 \rightarrow S_0$ transitions are shown in the electronic state scheme.

green arrow). Only one electron is unpaired so the overall spin is $\pm\frac{1}{2}$ which leaves the molecule in a doublet D_0 configuration. The molecule is subsequently excited by laser radiation, indicated as blue arrow, with a wavelength directly proportional to its energy E_{Photon}. If at any point the laser wavelength exceeds the detachment threshold an electron is emitted (turquoise arrows & e^-). The resulting electron's kinetic energy can then be expressed through a modified version of equation 6.14:

$$E_{kin,electron} = E_{Photon} - E_{S_0,v_i} \tag{6.16}$$

$E_{kin,electron}$ = kinectic energy of the electron, E_{Photon} = photon energy, E_{S_0} = energetic position of the S_0 state in its vibrational quantum state v_i

By rewriting the equation in terms of E_{S_0,v_i} the difference between the anion and the neutral ground state can be calculated. In its ground state, the anion always has an overall spin of $\pm\frac{1}{2}$ (doublet configuration). From here the ejected electron takes a spin of $\pm\frac{1}{2}$ from the molecule ($\Delta s = \pm\frac{1}{2}$). Therefore, it is possible to reach either singlet (s=0) or triplet (s=±1) states from the doublet D_0. Note that the number of reachable states is only limited by the maximum photon energy of the excitation laser. The equation to calculate these other, higher states is a simple expansion of equation 6.16. For example, the T_1 state can be calculated by:

$$E_{T_1} = E_{Photon} - EA - E_{kin,electron} \tag{6.17}$$

E_{T_1} = energetic position of the T_1 state in respect of the neutral ground state, E_{Photon} = photon energy, EA = electron affinity, $E_{kin,electron}$ = kinetic energy of the electron

Figure 6.5 displays the first three observable transitions to electronic states (S_0, T_1, S_1) in PD-PES. As all these states only differ from the

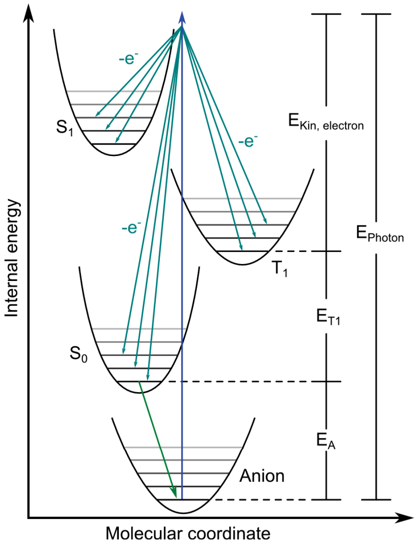

Figure 6.5.: Illustration of the processes in PD-PE spectroscopy (electronic state scheme). Detachment process only displayed schematically (Franck-Condon transition).

anion ground state by a spin of $\Delta s = \pm\frac{1}{2}$ they should all be reachable with the same probability if no other effects emerge. The main feature of this method is that virtually all transitions are allowed as the process of photo detachment merely resembles a fully dipole-allowed single photon ionization event in neutral spectroscopy.

6.4.3. Anion excited states

In some obvious cases the vibrational peaks and intensities of PD-PE spectra do not fully correlate with the expected anion-to-neutral Franck-Condon integral. As an example, figure 6.6 shows ground state S_0 spectra of *trans*-stilbene (SB). The spectrum displays two superim-

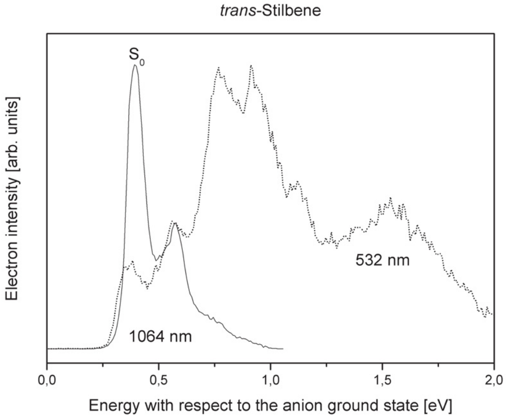

Figure 6.6.: PD-PE Spectra of *trans*-stilbene recorded with 1064 nm (solid line) and 532 nm (dotted line)[VS11]. Resonant excited anion states cause a modulation of the Franck-Condon factors to higher vibrations of the S_0 when detaching with 532 nm.

posed PD-PE spectra, recorded with detachment wavelength of 1064 nm (solid line) and 532 nm (dotted line). Theoretical calculations predict very low shifts in geometry between the anion and the neutral ground state. Therefore, it has to be expected that only one strong $0 \rightarrow 0$ origin appears, followed by just a few vibrational peaks. The spectrum measured with a detachment wavelength of 1064 nm exactly confirms this assumption, whereas in contrast to this the dotted line spectrum (532 nm detachment wavelength) exhibits strong additional spectral features. As no other transitions should be visible in this energy range the observed transitions must definitely belong to vibration of the S_0 ground state. This is also supported by the same spacing between the first/second peaks (also displayed at 1064 nm) and the third/fourth peak (only visible at 532 nm). Literature on absorption spectra[TAK74] states that SB anions posses a strong absorption band at 500 nm, very close to the detachment wavelength of 532 nm used here. Therefore, it is possible to excite this anion state with high probability. Because, as in this case, anion excited states often lie above the detachment threshold, electrons can be emitted spontaneously by autodetachment. Figure 6.7 shows these anionic resonances and the resulting autodetachment in the electronic state diagram. In consequence to this process the Franck-Condon factors from the anion ground state to neutral ground state transition do not apply as the probability of th alternate detachment process is only governed by the excited anion to neutral Franck-Condon factors. Hence it is obvious from the dramatic effects in figure 6.7 (532 nm excitation wavelength), that resonant excitations have a much higher cross-section than continuum transitions

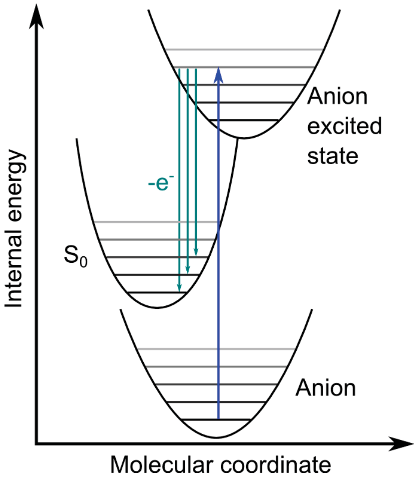

Figure 6.7.: Schematic diagram of transitions to anion excited states and subsequent autodetachment processes.

and have to be avoided to gain exact relative intensities of the vibrational peaks (see chapter 7.2.2).

7. Experimental setup

The experimental setup consists of the self-made mass and electron spectrometers, two modified, commercial ND:YAG-Lasers and and specially designed data acquisition and processing system. The following chapter will mainly focus on the spectrometer and its modifications.

7.1. Overview: The anion photo detachment photo electron spectrometer

The spectrometer used in this work is depicted in figure 7.1. It can roughly be divided into three sections: The inlet system in vacuum chamber I, the mass spectrometer from chamber II to chamber IV and the two electron spectrometers in chamber V and VI. The vacuum system itself will not be covered in detail in this text as it would only distract the reader from the matters at hand. In short, it consist of six differentially pumped vacuum chambers, which are connected through a skimmer between chamber I and II and small openings (as pressure barriers) between chambers II/III and III/IV. To facilitate rapid sample changing and technical modifications in one of the first four chambers an additional high vacuum electro-pneumatic valve was installed between the mass and electron spectrometer. To avoid oil contamination, all stages are pumped either by turbomolecular or cryo pumps.

7.1.1. Inlet systems

For injection of the sample molecules in the spectrometer a thermal vaporisation source with jet-cooling, after electron attachment in a supersonic expansion, was chosen. The main inlet system consists of a highly modified heated pulse-nozzle (General Valve Series 9), which in-

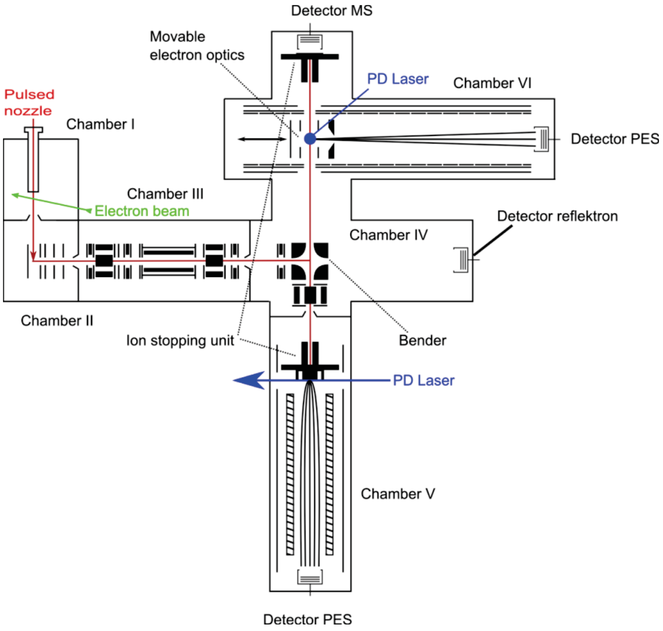

Figure 7.1.: Schematic diagram of the apparatus with inlet chamber (I), linear ToF mass spectrometer (II-IV) and both magnetic bottle (V) and electrostatic (IV) PD-PE spectrometer .

jects neutral molecules into the vacuum chamber. The sample molecules are stored in an small compartment in the nozzle head. This allows the use of both solid and liquid samples. Additionally it opens up the possibility to degas the sample prior to heating. The heating is done by an electrical coil which is directly coupled to the nozzle head. Special care had to be taken to ensure a magnetic and electric field-free heating coil. Therefore, electrically insolated and bifilar-wound core heating elements were used.

High temperature nozzle modifications

To measure samples with high sublimation temperatures special modification to the nozzle system had to be made. The original system consisted of a solenoid, a ferrite-core plunger and a short Vespel® poppet which were directly placed into the nozzle head. All joints were sealed by fluoroelastomer (FKM) gaskets. The energized solenoid pulled the plunger upwards and the attached poppet released the nozzle head's orifice. Then, two springs moved plunger and poppet back into the starting position.

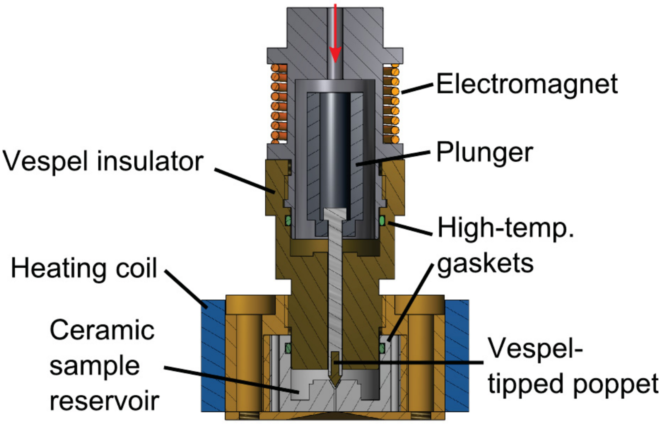

Figure 7.2.: Modified high-temperature nozzle. Simplified version without springs.

However, standard General Valve pulse-nozzles are only capable of withstanding temperatures of about 475 to 500 K. As the solenoid is especially vulnerable to higher temperatures an additional Vespel® spacer had to be inserted between the nozzle head and the coil's bobbin. For this the poppet also had to be extended by a factor of two. This led to a problematic situation with sporadic pulse dropouts of the nozzle, caused by softening of the long plastic poppet at about 553 K. To counter this shortcoming a new two-part poppet was designed. Its main body consists of aluminum, which is temperature-stable as well as light. The only drawback is that leak-free dynamic metal-to-metal sealings between the poppet and the nozzles pin-hole are difficult to produce. To act as an elastic sealant the tip of the aluminum poppet was hollowed-out and a small Vespel® peg was inserted into the resulting bore. To counter the effects of sample decomposition and temperature induced reactions in the nozzle, all metallic surfaces in contact with the sample were replaced with non-catalytic materials. Therefore, a ceramic inlay was inserted into the nozzles head.

Additional, all o-ring sealed joints were sealed by custom designed perfluoroelastomer (FFKM) gaskets. These modifications now allow temperatures up to about 590 K and were successfully applied in the study of sexithiophene by Siegert et al.[SIE10, SV11b].

7.1.2. Anion formation

This work uses radical anions formed by electron attachment for the spectroscopy of closed shell neutrals. In nearly all electrostatic mass spectrometers, ionization of the (gaseous) sample molecules is the first step. As this work focuses on the spectroscopy of anions, negative charged sample particles have to be produced. One of the easiest ways to generate anions would be electrospray ionization (ESI). In ESI, sample molecule solutions are simultaneously gasified and ionized due to an high electrostatic field. Anions are formed by abstraction of acidic protons; therefore, most of the anions are deprotonated closed-shell molecules. Recent experiments by Fu et al. showed that in special cases also open shell radical anions, albeit in very small quantities, could be produced[FU11]. As PD-PE spectroscopy heavily relies on high radical anion counts, electrospray ionization is not well suited for such experiments. To ensure high amounts of open-shell anions, direct electron attachment to neutral molecules in the gas phase is used. It is obvious that this process is only possible if the sample has a positive electron affinity, so electrons can be attached with a gain in energy. Also, as the attachment cross-section is inversely proportional to the electrons energy[KLA92], only low energy electrons can be attached to the neutral sample molecules. Therefore, high energy electrons from an electron gun cannot be used directly. To create low energy electrons, a primary high energy electron beam is crossed with the carrier gas molecules (N_2[BRU67] at 1.6 MPa). These low-energetic electrons can then attach to the neutral sample molecules in the carrier gas. Typically, only a small numbers of sample molecule should be present in the carrier gas to prevent high fragmentation counts. Since in the first step of the electron attachment process the energy is conserved, the anions are formed in very high vibronic states or via anion excited states. The electron affinity, i.e., the electron binding energy, is converted into internal vibrational energy. From there the resulting vibronic excess energy in the anion (excited) state has to be cooled down subsequently to reach the anion ground state. As electron attachment is still a rather inefficient process, many high-energetic electrons have to be produced to ensure a high density of low-energetic electrons. Standard electron guns, albeit highly improved over the years, cannot satisfy this need at heavy carrier gas pulses and the resulting operating chamber pressures. Therefore, a pulsed high pressure, high yield micro channel plate (MCP) electron gun was incorporated into the design[SCH99b]. Figure 7.3 displays a schematic illustration of the different parts of the electron source.

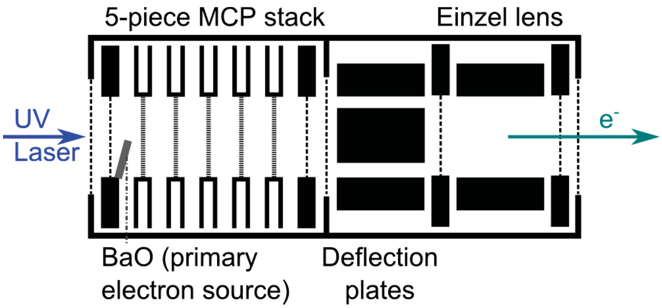

Figure 7.3.: UV laser-seeded micro-channel plate electron gun as source for primary electrons. Amplified electron current is emitted to the right. Carrier gas is ionized to create low energy secondary electrons for electron attachment. Maximum pulsed current of 5 mA over a duration of 200 ns was achieved. A primary source of electrons before amplification a BaO rod was included in the electron gun.

First, a laser pulse (266 nm, 20 ns pulselength) creates the first few electrons from a bariumoxide (BaO) covered surface. Bariumoxide was chosen for its low work function, vacuum fitness and high availability. From here the electrons are accelerated onto a microchannel plate stack to amplify the electron current. The whole electron multiplier unit consist of a stack of 5 microchannel plates (For information on MCP electron multipliers see section 7.1.4). These plates were cut with a laser to fit into the small housing of the electron gun and to ensure a good spatial overlap between the individual multiplication stages. The last plates was cut from a high gain, high current type MCP to maximize electron output. Each plate achieves a multiplication factor of about 10^3; therefore, theoretically, one primary seed photon generates an overall output of 10^{15} electrons. Additional deflection and focusing units allow the accelerated (about 1 to 1.5 keV) electron beam to be precisely aligned to the nozzle head and into the molecular beam.

7.1.3. Mass selection

The actual mass selection is performed in an modified Wiley-McLaren time-of-flight mass spectrometer. The anions are therefore injected into the anion source through a skimmer between first two chambers. In 1955, Wiley and McLaren[WIL55] discussed the errors in flight time in a linear time-of-flight mass spectrometer. Ions of the same mass often suffer from different arrival times at the detector, due to different ion formation times, spatial distribution in the ion source and their initial kinetic energy. To compensate a pulsed two-grid ion source was incorporated in the design, so later formed ions could catch up with the earlier ones and spatial distribution would be reduced. This first order correction negates all errors emerging from different starting positions. To achieve higher order corrections[WEI89] special dimensions of the ion source were needed. As different kinetic energies of one mass would broaden the electron spectra, ion source pulse focusing[VOG09], a special type of variable impulse field focusing[BRO81], was used. A quadrupole bender then further improves mass selection by additional mass gating.

7.1.4. Ion detection

To be able to measure mass spectra, the exact arrival times of the resulting mass selected ion cloud have to be measured. Hence, the incoming ions have to be converted to a processable electrical signal. A Faraday cup is an easy apparatus to detect absolute number charged particles[BRO56]. The particles are, therefore, accelerated and strike a metal surface which can be discharged and measured through a high impedance pathway. The main advantages of this method are its mass independence and the direct proportionality to the ion count given by equation 7.1.

$$\frac{N}{t} = \frac{I}{e} \tag{7.1}$$

$\frac{N}{t}$ = Number of particles N per duration t, I = measured electrical current, e = elementary charge $1.60 \times 10^{-19} C$

As this system lacks sensitivity and temporal resolution it is often substituted with other methods like secondary emission electron multipliers (SEM). In a SEM a single ion or electron is accelerated onto a coated plate (secondary emissive materials) were multiple secondary electrons are emitted[ALL39, ALL47]. Again these are accelerated onto the next plate of the SEM where the next electrons are released. Combining many of these multiplication stages allows amplification of a single electron up to 10^7 resulting electrons. The main problem with this approach is, that extended and bulky plate arrays induce a high time spread in electron flight paths and hence broadens the signal. To minimize this time spread, caused by the different pathways through the detector, the path between the different multiplication plates has to be minimized while maintaining a high number of multiplication stages. Microchannel plates are especially designed for this task. They consist of many small ($\approx$10μm) parallel channels, which each resembling one highly miniaturized secondary electron multiplier. Figure 7.4 shows a lateral cut through the profile of a microchannel plate. With a detector build from two of these microchannel plates, an additional high impedance anode and a capacitor-decoupled 50 Ω output, it is possible to detect even single electrons while still maintaining sub-nanosecond response times.

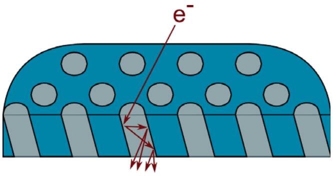

Figure 7.4.: Lateral cut through the profile of a microchannel plate. Electrons are displayed as red arrows.

7.2. The electron spectrometers

Photoelectron spectrometers are delicate machines because the flight path of the light electron are easily disturbed by electric and magnetic fields. Resolution (given in ΔE) and transmission are typically mutually exclusive.
Many different types of electron spectrometers (field-free ToF, magnetic bottle, ZEKE and SEVI) were developed throughout the last century. As Siegert gave an exhaustive in his work[SIE10] only the two types of photodetachment photoelectron spectrometers used in this work, will be covered here. These include the:

- Magnetic bottle spectrometer (low-resolution, high collection efficiency)
- Electrostatic time-of-flight spectrometer (high-resolution, low collection efficiency)
  - Field-free operation
  - Electrostatic electron deceleration mode

The magnetic bottle spectrometer was constructed first and was later upgraded with an electrostatic time-of-flight spectrometer to overcome its resolution limitations. It is now primarily used for low resolution overview spectra of formerly unmeasured substances. Its main advantage is the ability to quickly record spectra with different wavelengths to recognize anion excited states. As anion excited often exhibit abnormally modulated vibronic patterns and a high broadening of the peaks only a low resolution is needed. To measure high resolution spectra the field-free electrostatic time-of-flight spectrometer is used and, if the electrons intensity permits, the maximum spectral resolution can be achieved in the electron deceleration mode.

7.2.1. The magnetic bottle electron spectrometer

Field-free photodetachment photoelectron spectrometers typically suffer from relatively small electron collection efficiencies as no efforts are taken to increase the number of detected electrons other than ensuring a perfect zero-field and collision-free spectrometer. For example, for a one meter long drifting distance, the collection efficiency drops down to about 5×10^{-4}, because only those electrons are detected which are incidentally emitted into the direction of the flight path and towards the detector. This often prolongs recording times for the spectra, making it difficult to stabilize the parameters throughout the whole experiment. As increased anion currents for compensation of low transmission would result in space charge effects for ions and electrons, another solution was chosen. Therefore, in this work a magnetic bottle electron spectrometer was used to simultaneously increase the collection efficiency and decrease the recording time. The main idea of a magnetic bottle is to guide all electrons with a spatial highly divergent magnetic field towards the detector. The first implementation of such a design was in 1983 by Kruit and Read[KRU83]. Although the initial experiment was flawed it was later improved by Cheshnovsky[CHE87]. To ease the generation of the magnetic field Gantefór et al. used permanent magnets[GAN88a, GAN88b] instead of electromagnetic coils. Further improvement were carried out by Handschuh and Wang[HAN95, WAN99]. Recent developments by Cheshnovsky and co-workers[GIN01], based on former works[MAR91a, MAR91b, MAR94], improved the collection efficiency to a near 4π collection sphere with up to 98 percent of the detached electrons focused on the detector. Resolution improvements up to 15 meV for organic substances were achieved. For this the highly divergent magnetic field was generated by a fast pulsed solenoid. The electrons were detached between the solenoid and the flight tube. A short electric pulse applied to the solenoid coils bobbin then decelerated all electrons resulting in lower peak broadening due to initial velocity of the ions. The magnetic bottle used in this work tried an alternate approach to

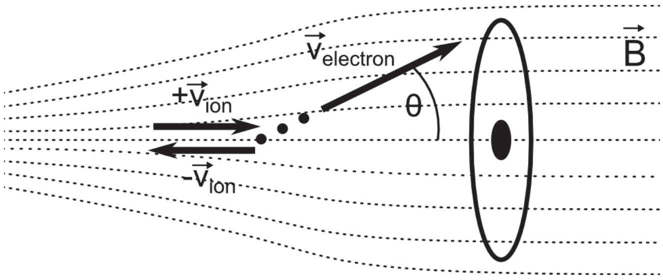

Figure 7.5.: Schematic view of the magnetic bottle principle taken from Giniger et al.[GIN01]. Superposition of the ion velocity $\pm v_{ion}$ and the velocity $v_{electron}$ of the detached electron. Θ is the angle between the symmetry axis and the resulting electron flight vector. In this setup the v_{ion} is coaxial with the electron flight path and the magnetic field lines.

counter ion-induced broadening. As the ion velocity is directly proportional to the peak width, a reduced speed should lead to higher resolution if no other effects interfere. Accordingly a stopping unit (see figure 7.1 on page 32 for further information) was incorporated into a permanent magnet design[GAN88a, GAN88b]. After the ions have drifted into the stopping unit[HAN95], a variable high voltage is applied to its outer hull. The inside of the stopping unit is field-free so the ions are subjected to an electrostatic force upon leaving. There, all ions are decelerated before being detached. The maximum achieved electron energy resolution for this setup was about 25 meV. Ideally the velocity of the ions should be decreased to zero to further increase in resolution, but since many ions are lost in the process this is not feasible. Because it turned out that the recording of high resolution spectra is impossible with the magnetic bottle, another field-free electron spectrometer (with its low collection efficiency) was added to the setup.

When the resolution is of minor importance, e.g., for quick overview spectra, the magnetic bottle is still used despite its low resolution of about 25 meV. The interesting spectral ranges are then investigated in more detail by the high resolution spectrometer.

7.2.2. The electrostatic time-of-flight photo electron spectrometer

For systematic assignment of the excited states in neutral molecules it is necessary to distinguish between tightly spaced electronic states and assign their respective vibronic levels. Especially for nπ^* transitions, where the singlet-triplet splitting is often smaller than 5 meV it is necessary to reach high electron resolutions. As magnetic bottles cannot fulfill this prerequisite and velocity-map imaging system are costly and require frequent calibrations an electrostatic electron spectrometer was chosen for this task. Based on the combined theoretical background described in chapter 6.3.1 and 6.4.2, a field-free time-of-flight electron spectrometer operates similar to a time-of-flight mass spectrometer except that the mass is constant and the energies are different. The ions are therefore struck by a laser pulse in a electrostatic and magnetic field-free region. The resulting electrons then drift into random directions. The ions are still moving during photodetachment, so the reference system for the electrons is moving too. Therefore all electron velocities (given by $velocity = \frac{distance}{flight\ duration}$) have to be transformed into a fixed reference system by:

$$v_{e^-,fix} = \sqrt{v_{e^-,mov}^2 + v_{ion}^2} \tag{7.2}$$

$v_{e^-,fix}$ = velocity of the electron in the fixed reference system, $v_{e^-,mov}$ = velocity of the electron in the moving reference system (measured with TOF), v_{ion} = velocity of the ions

Figure 7.6 shows the relation between $v_{e^-,fix}$, $v_{e^-,mov}$ and v_{ion} in a the geometric translation based on the intercept theorem. This creates an intrinsic systematical shift in the electrons flight time, which can easily be eliminated computationally.

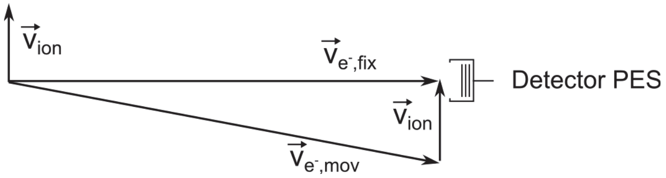

Figure 7.6.: Geometric correlation between the ion velocity v_{ion} and the electron's velocity in the fixed $v_{e^-,fix}$ and moving $v_{e^-,mov}$ system based on the intercept theorem. Taken from [SCH98].

To calculate the overall resolution error (broadening of the peaks, no shifting!) all effects distorting the electrons velocity or flight distance have to be included in the assessment. The three major effect influences that apply here are:

- Geometrical effects
- Timing effect
- Electrostatic and magnetic field effects

The whole energy deviation can be described by the following equation:

$$\frac{\Delta E}{E} = \sqrt{\left(\frac{\Delta E_x}{E}\right)^2 + \left(\frac{\Delta E_t}{E}\right)^2 + \left(\frac{\Delta E_\lambda}{E}\right)^2 + \left(\frac{\Delta E_v}{E}\right)^2} \tag{7.3}$$

ΔE = energy resolution, E = electron energy, other terms are energy errors: ΔE_x = path differences, ΔE_t = laser pulse width and timing errors , ΔE_λ = uncertainty of the laser wavelength and ΔE_v = error in the electrons speed, e.g., by stray fields (taken from [SCH98])

ΔE_x includes all errors induced through path differences. Mainly two sources of errors apply here. First the laser ion interaction volume: No laser system has an infinitesimal small focus, so the starting position is not confined to one point in space. Therefore, the distance between the detachment site and the detector differs by one or two millimeters for all electrons. The detector itself also has a certain dimension of about 20 mm radius from the central electronic coupling point. So all electrons not striking the detector at the same distance from the center have a slightly longer flight path. Fortunately, path differences apply with respect to the overall flight length which is by about three magnitudes larger, efficiently mitigating these errors.

The laser pulse width (ΔE_t, timing errors) of about 7-8 ns induces a large error when measuring electrons with high kinetic energies. Thus, electron excess energy has to be decreased by either selecting a longer detachment wavelength with a dye laser or decelerating the kinetic electrons with electrostatic field (see chapter 7.2.2 for further information).

Another option, not implemented at the moment, would be to shorten the laser pulses with additional Pockels-cells to reduce its influence on the resolution. Timing errors triggered by all kinds of jitter or runaways of timed delays, faulty cabling or ground loops should be avoidable by careful selection and maintenance of the employed equipment. As modern seeded Nd:YAG laser as well as dye lasers provide good stability and small linewidth deviations, the errors caused by the laser system (ΔE_λ) are neglectable. All other uncertainties are mainly caused by errors in the electron velocities, imposed by stray fields. Electrons might be influenced on the flight path by residual electric and/or magnetic fields so their initial energy and flight duration changes. One of the more common causes for electrostatic fields are the inhomogeneities in the surfaces of the spectrometer. Special care had to be taken to create a field-free surface by covering the inner sections of the spectrometer in thinly sprayed colloidal graphite layers. This ensures a fully electrostatic homogeneous surface, free of different contact potentials. Uniform coverage with the remaining water molecules was achieved by constant heating of the graphite coated inner aluminum tube to about 372 K. Consequently, the attached heating coil was bifilar wound to avoid electromagnetic effects. To shield the flight path from earth's magnetic field dual μ-metal shielding was layered around the heated aluminum tube core. This decreased the magnetic field in the flight tube to about 300 nT[SCH98]. Detector and laser access were shielded by dual meshes and light baffles. The resulting electron flight path of 817 mm now causes a transmission efficiency of about 10^{-4}. This low transmission usually prohibits any spatial or temporal laser adjustment as a significant amount of signal per second is needed to allow a validation of the system's parameters. To conquer this problem a movable electron optics was developed to increase transmission efficiency.

Movable electron optics

As mentioned before spatial and temporal adjustments play an important role in measuring high resolution PD-PE spectra of anions. So adjusting the anion molecular beam has to be done as precisely and repeatable as possible. This especially holds true for measurements with extremely low anion counts and/or low photodetachment cross-sections. Firing the laser at incorrect times, i.e., not into the most dense part of the anion cloud, generates extreme high measurement durations. As low electron intensities make the setup rather tedious if not impossible, a new adjustment system had to be incorporated into the spectrometer. To boost electron intensity a special electron acceleration optics was installed into the electron flight tube, which forces all electron onto the detector. Figure 7.7 shows a more detailed version of the field-free anion photo electron spectrometer. The left side (labeled 'a)') of the drawing shows the spectrometer in its high electron collection mode, where a voltage is applied to the first plate of a three plate electron acceleration optics. This resulting electrostatic field directs all emitted electron from the detachment site to the electron detector. Only low voltages are needed to accomplish significant changes in the anion flight path and deflect all electron in a 90° angle to the detector. However,

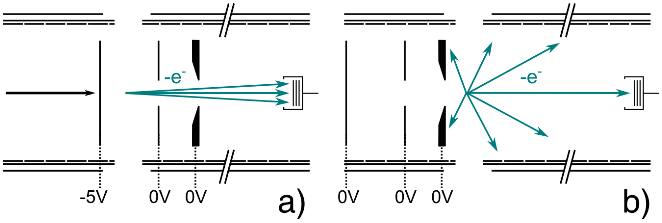

Figure 7.7.: Schematic diagram of the photodetachment site with and without the movable electron optics.

as any surfaces near the photodetachment site broaden the spectra, the optics had to be made retractable to ensure a field-free environment for the electrons during the measurements. This setup also allows to counter one of the main problems in radical anion spectroscopy, the anion excited states.

Since up to now only few electronic anion resonances have been measured, most of the excited state transitions, needed to understand PD-PE spectra, cannot be found in literature. To counter the problem of anionic excited states a different, non-resonant, excitation wavelength should be used. It is often impractical to scan large wavelength intervals with dye lasers due to small bandwidth of the dyes causing frequent readjustments of the system. On the other hand optical parametric oscillators (OPO) though being able to be easily scanned over large intervals, often suffer from broad linewidths when used in high output systems. Therefore, in this work, the different harmonic wavelengths of a Nd:YAG laser were used to distinguish between normal and anion excited state induced peaks. Due to the large photon energy spacing of the available wavelegths, it was not always possible to use a wavelength with a resulting low electron excess energy. As mentioned before the excess energy of the electrons also determines the resolution of the spectra. To mitigate broadening, the high kinetic energy of the electrons has to be reduced, in other words the high speed electrons have to be slowed down. The newly introduced electron optics satisfies this need for a decelerating electrostatic field. For this, the electron optics has to be moved to the position shown in figure 7.7 ‘a)’. The electrons are detached between the first and the second plate, which are both held at the same (positive) potential. This assures that the electrons are ejected in a field-free region and their final energy does not depend on their position in the electron optics. All electrons which leave the

electron optics in direction of the detector are therefore decelerated by the attractive field between the second and the third plate.
To show the results of this setup the spectra of xanthone are shown in figure 7.8. The figure shows two superimposed PD-PE spectra. Both display the S_0 ground state of xanthone. The black spectrum was recorded with 1064 nm. It shows a strong influence of anion excited states as the intensities of the peaks clearly do not comply with anion ground state to neutral ground state Franck-Condon factors of the active modes. The red spectrum, recorded with 532 nm, shows the same vibrational pattern as the other one, but with plausible intensities according to the Franck-Condon principle. Also it is noteworthy that through deceleration of the high energetic electrons it was possible to achieve the same resolution as in the black spectrum. Therefore, it

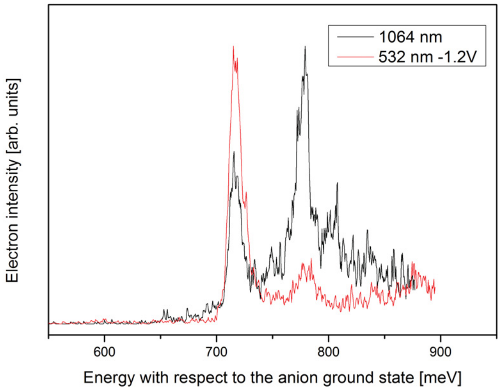

Figure 7.8.: PD-PE spectra of the S_0 state of xanthone recorded with 1064 and 532 nm. Note the influence of an anion excited state on the detachment Franck-Condon factor.

can be stated that this method is especially well suited to anticipate anionic resonances while still maintaining high spectral resolution. In a variation of this method, VUV-wavelengths (F_2 laser/HeI) in combination with electron deceleration could be used, to completely eliminate all anionic resonances.

7.2.3. Calibration of the PD-PE spectrometer

Beside its high resolution, ToF-PES does not need new calibration for each recorded spectrum if a field-free flight path is realized. For an initial, one-time calibration of the field-free time-of-flight electron spectrometer, atomic iodine anions were used. Electronic transitions in atoms should only display one single peak as no vibrations or rotations exist. Therefore, the peakwidth of the resulting spectrum should solely depend on the resolution of the spectrometer. The electron affinity was

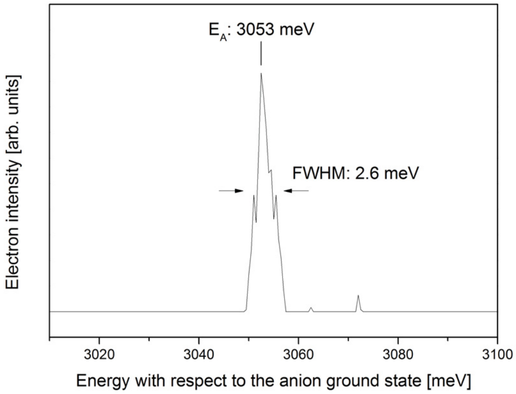

Figure 7.9.: PD-PES of the iodine atom anion. An EA of 3053 meV[HAN92, PEL09] was determined with a resolution of 2.6 meV.

measured to be 3053 meV as shown in figure 7.9 with an overall resolution of 2.6 meV. The absolute position is in good agreement with literature data measured by Hanstorp et al. in 1992 (3.059038±0.000010 eV[HAN92]) and Pelaez et al. in 2009 (3.0590463(38)±0.00010 [PEL09]). Only one peak is visible due to large gap between lower ($J = \frac{3}{2}$) and upper ($J = \frac{1}{2}$, 7603.15 cm^{-1}) spin-orbit component[MIN62].

8. Results and discussion

To show the merits of radical anion photodetachment photoelectron spectroscopy for dark states of organic molecules, two different classes of organic systems were chosen: aromatic hydrocarbon polyenes and heteroaromatic organic substances. This chapter will give detailed informations about the findings and discuss their implication on photophysical and photochemical mechanisms.

8.1. Heteroaromatic nπ* states

Heteroaromats are aromatic π systems where a part of the carbon ring system is substituted with other heteroatoms in such a way that the conjugation of the π system is preserved. Like benzene they are characterized by $4n + 2$ (n = number of atoms in the π system) cyclic conjugated electrons in the π system. These heteroatoms often feature lone-pair electrons perpendicular to the π electron cloud. In the 1960s, El-Sayed and co-workers identified some special transition properties about these lone-pair n orbitals[ELS63, LOW66, ELS68]. El-Sayed's rule states that intersystem crossing rates (ISC: a low yield photophysical process involving an isoenergetic radiation-less transition between two electronic states of different multiplicities) can significantly be enhanced by involvement of a change in molecular orbital type during the radiation-less transition. For example, a singlet $\pi\pi$* state can interconvert population into a triplet nπ* state, but not to a triplet $\pi\pi$* state and vice versa. Therefore, in aromatic carbonyl compounds, the ISC deactivation process can happen on the low nano- to picoseconds timescale rivaling singlet relaxation pathways. Vibrational coupling to out-of-plane modes potentiate this effect[REN70, LIR77]. As most nπ*

states only exhibit low transition probabilities and are easily shifted by solvation effects[BAR75], extensive studies are often problematic.

8.2. p-Benzoquinone[SV11a]

For this work, *p*-benzoquinone (pBQ, see figure 8.1 for chemical structure) was chosen as a test molecule for first nπ* studies on smaller (hetero-)substituted aromatic molecules (the herein shown findings are reproduced from reference [SV11a], in an independent study Fu et al. did an similar study on *o*-, *m*- and *p*-benzoquinone[FU11] however being more focused on theoretical and structural calculations). This aromatic diketone often serves as motif found in natural systems. The most prominent example is ubiquinone, or Coenzyme Q_{10}, which plays an important role in both the electron transport chain (ETC)[ERN95], as electron or proton transmitter, and in photosynthesis as final electron acceptor[VOE95]. pBQ and its derivatives have been in the focus of experimental[KOY70, VEE73, THO79, ALL84, ITO95] and theoretical[WOO75] [HA83, PAM99, WEB01] studies since the early 1970s. Many of the former works show that in the first electronic states of pBQ special photophysical properties occur:

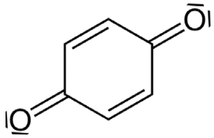

Figure 8.1.: Chemical structure of *p*-benzoquinone.

- The first six electronic transitions are all forbidden[WEB01] by spin selection rules. Moreover, in many transition two or more selection rules apply at the same time. A good example for this is the first excited triplet state T_1, where the transition is prohibited by spin inversion (*singlet* → *triplet*), Laporte's rule ($1^1A_g \rightarrow 1^3B_{1g}$) and also $n \rightarrow \pi^*$ selection rules. See chapter 6.2 on page 12 for further information.

- The energetic order of the electronic states does not cohere to the order of the orbitals in the MO scheme.
- The lone-pair state combinations n_+ and n_- on the oxygen atoms are very close in energy, therefore singlet-triplet splitting between the S_1, S_2 and T_1, T_2 states should be small. If also a third predicted triplet state (postulated by [WOO75, HA83, WEB01]) is additionally taken into account, the state density in this energy range should be extremely high.
- Finally the stabilization of the surplus electron in radical anions of *p*-benzoquinone. pBQ displays a rather high electron affinity of about 1.86 eV[SCH99, SV11a], which cannot only be attributed to the molecule's π system and substituents. pBQ is capable of efficiently capturing electrons with energies of about 2 eV[COO75] and by this creating long-term stable open-shell anions. In addition pBQ also shows signs of delayed autodetachment from anion excited state[COO75, MAR85, SCH99].

To be able to understand all implications with these special photophysical properties, the MO scheme of pBQ is compared to its associated electronic state scheme. Part a) of figure 8.2 shows the MO scheme of *p*-benzoquinone with its non-bonding lone-pair orbitals (n_+ and nn_-) situated below the bonding π orbitals ($H = HOMO$ and $H-1 = HOMO-1$). Part b) shows the corresponding electronic state scheme according to past studies on pBQ. The ordering mainly relies on theoretical data[WOO75, HA83, WEB01] as most experimental works[ALL84]

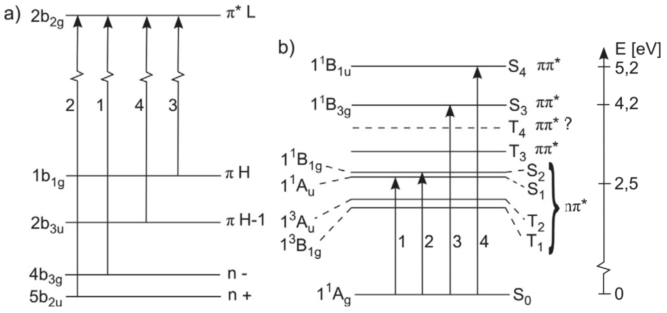

Figure 8.2.: MO a) and electronic state b) scheme of *p*-benzoquinone as described in past experiments (for references see text). 1,2,3 and 4 denote the corresponding transitions in the MO and electronic state scheme. The inversed order of the different transitions shows that in pBQ the electron configuration in the MO scheme does not reflect the final energetic configuration of the excited electronic states. Here the transition between $n_- \rightarrow \pi^*_{L=LUMO}$ lies in the VIS area whereas $\pi_{H=HOMO} \rightarrow \pi^*_{LUMO}$ in the UV range.

do not fully account for the T_3 and T_4 states. In [WEB01] a different order for T_1, T_2, S_1 an S_2 was proposed. As this theoretical findings could not be verified experimentally, this ordering of the lowest singlet and triplet states is not used here. In this work also three additional singlet states and a not further specified number of triplet states are predicted to lie below the first optical accessible state(proposed: S_4) with 1^1B_{1u} symmetry. 1,2,3 and 4 denote the corresponding transitions in the MO and electronic state scheme. At first look each scheme for itself makes sense, but once combined the discrepancy becomes directly visible. To further explain this mismatch between the schemes in detail, one has to focus on the energetic order of transitions 1 & 2 and 3 & 4. In figure 8.2 b) the length of the different vertical arrows shows that transitions

1 and 2 are much lower in energy that transitions 3 and 4, whereas in figure 8.2 a) transition 1 and 2 seem to be much higher in energy than 3 and 4. Therefore it is clear that the MO scheme does only show the molecular orbitals before excitation and by no means the resulting energy differences depicted in the electronic state scheme. So the MO scheme only displays a mere static picture of the molecular orbitals, not accounting for energetic shifts and reordering of the molecular orbitals in case of changes in population. In pBQ these shifts are caused by a large quadrupole moment in the S_0 ground state described by Schiedt et al. in 1999[SCH99]. When the negative charge is transferred from the oxygen lone-pair $n_{+/-}$ orbital to the π^* orbital of the aromatic system, this quadrupole moment is lost, due to charge equilibration. This effect is non-existent for $\pi\pi^*$ states as no coulombic stabilization occurs. Interestingly, nearly all low-lying electronic states in *p*-benzoquinone are dark states, induced by one or another selection rule. Therefore in the neutral molecule the only way for these states to gain intensity is by the vibronic Renner-Herzberg-Teller coupling to near transition-allowed electronic states. In consequence, sophisticated methods have to be employed to assign the electronic origins for those states. An often applied method is the vibronic extrapolation of 'false origins'. The problem here is that in pBQ many different electronic states are situated in a small energy range, so many vibrations overlap, making it nearly impossible to assign them to the different electronic states. Only the S_1 state could be investigated with reasonable certainty by means of such an approach. As the S_0 to S_2 transition is electric-dipole forbidden, but magnetic-dipole allowed the transition energy could tentatively be assigned to 2.49 eV[THO79]. From there it was possible to indirectly locate the S_1 at 2,48 eV, about 54 cm^{-1} lower by vibrational analysis[THO79].

To locate the lowest triplet states, solid phase crystal absorption and dispersed phosphorescence at very low temperatures were utilized to obtain a S_0 to T_1 transition of 2.31 eV[KOY70]. From there the T_2 state could be measured with a triplet-triplet absorption energy ($T_1 \rightarrow T_2$) of 320 cm^{-1}[VEE73]. The problem with these values is that almost all solid phase crystal data suffers from inherent shifts imposed by environmental effects[WEB01], especially with strong quadrupole moments present in pBQ (blue shift predicted). To be able to determine the $n\pi^*$ states with higher certainty Allan, in 1984 applied electron energy loss spectroscopy (EELS) to this problem[ALL84]. Normally EELS is a perfectly suited method for measuring forbidden neutral states, especially triplet states. It is often even possible to directly distinguish between singlet and triplet by varying primary electron energy and incident angle. However, in this case, it was not feasible to define whether the peaks were caused by $n\pi^*$ or other $\pi\pi^*$[WOO75, HA83, WEB01] transitions. Therefore it was not possible to fully determine the origin of the transition in the 3 eV (peak maximum) range. The big problem with $n\pi^*$ states in EEL spectroscopy here, was the low interaction cross-section of the compact n orbitals with the primary electrons, leading to very weak spectral features and intensities. This work now aims to clarify the different former findings by others through measuring dipole-forbidden $n\pi^*$ states with photo detachment photo electron spectroscopy[SV11a].

In figure 8.3 the gas phase PD-PE spectrum (left side trace) of *p*-benzoquinone is compared to its corresponding liquid phase UV-VIS spectrum (right side trace) in hexane. The PD-PE spectra were recorded with 532 nm and 212,8 nm, to accommodate for the higher resolution with different detachment energies. The break is indicated by the gray marking at about 2.6 eV (anionic energy scale). It was possible to reach an overall resolution of about 40 meV and an absolute accuracy of 30

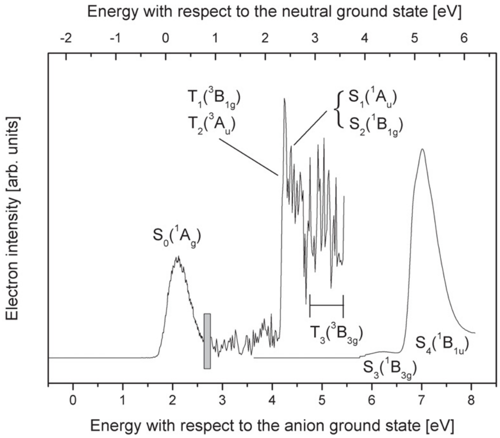

Figure 8.3.: PD-PE (left spectrum) and liquid phase UV-VIS in hexane (right spectrum) spectra of *p*-benzoquinone. The PD-PES were recorded with 532 nm and 212,8 nm; joints are indicated by gray marking. To adapt UV-VIS to PD-PES data, the UV spectrum was shifted by 1.86 eV (electron affinity of pBQ). nπ* T_1 at 2.38 eV (neutral energy) and higher triplet and singlet states between 2.3 to 3.5 eV (neutral energy) are visible. Broad structure between 2.8 and 3.5 eV with respect to the neutral ground state indicate another forbidden state T_3 in this energy range.

meV. Both PD-PE spectra were measured with the magnetic bottle electron spectrometer. To adapt UV-VIS to PD-PE data, the UV spectrum was shifted up by 1.86 eV (electron affinity of pBQ).
The first fully transition allowed state is the S_4 (1^1B_{1u}), as indicated in the UV spectrum, with an ϵ of about $2{\times}10^4$[PER66]. The other visible state, the S_3 (1^1B_{3g}) is symmetry forbidden $(g \rightarrow g)$ by Laportes rule and therefore weak. Its intensity is mainly caused by vibronic Renner-Herzberg-Teller coupling to the nearby S_4 state. Note that the UV-VIS

spectrum shows no evidence of either S_1 or S_2 because of their low absorption coefficients of about 20[PER66]. The PD-PE spectrum shown in this work now displays its first state, the S_0 (1^1A_g) ground state, at 1.8 eV consistent with Schiedt et al.[SCH99]. This value now defines the shift for the neutral energy scale displayed on top of figure 8.3. For ease of comparing PD-PE and former neutral data, energies in respect of the neutral ground state will be used from here on.

The first neutral excited electronic state in the PD-PE spectrum is the signal rise at 2.38 eV which correlates very well to the T_1 state found in low-temperature crystals (2.308 eV from [THO79]). The small redshift of the crystal data can be explained by environmental effects in solid state experiments. Further analysis of the energy range between 2.3 eV and 3.5 eV shows that the interpretation of the displayed spectral structures can be rather tedious. High electronic state density and the resulting high vibrational overlap in combination with low resolution prohibit a fully qualified assertion about the order of the electronic states. Nevertheless this findings show that PD-PE spectroscopy is a well suited method for spectroscopy of transition forbidden $n\pi^*$ states. To further improve the usefulness of the recorded data it would be important to greatly increase the resolution of the gathered spectra to a sub-meV scale. A first step was taking by incorporating the additional field-free time-of-flight electron spectrometer in the setup. The resolution of this spectrometer has been determined according to chapter 7.2.3. Anyhow, as pBQ only exhibits a very low photodetachment cross-section, the main problem of field-free electron spectrometers, the low collection efficiency for the detached electrons, prohibits the application of this method at the moment.

Since radical anions have a doublet ground state with a resulting overall electron spin of $\pm\frac{1}{2}$, singlet and triplet states should be accessible with same spectral intensities through the removal of a single electron[SV11b]. As explained in chapter 6.2.1 one photon can only interact with one electron, therefore each neutral electronic states should have a predetermined electronic configurations. This limitation is directly imposed by the PD-PE method by positioning the surplus electron in the π^* LUMO orbital. During photo detachment the ejected electron carries its orbital symmetry, accordingly changing the orbital symmetry. Thus, if no other symmetry selection rules interfere with PD-PE spectroscopy (proven by the appearance of the T_1), there is no obvious reason that either T_2, S_1 or S_2 should not be present in our spectra.

The spectrum also clearly shows that a much higher resolution is needed to facilitate a well-defined conclusion on the order and position of the lowest excited electronic states in *p*-benzoquinone. Up to now the the problem of the large singlet-triplet splitting for the $\pi\pi^*$ transition was totally implausible and is now resolved by the experimental finding of the low-lying fifth triplet state.

8.3. Xanthone and its derivatives

Similar to oxygen substituted aromatic molecules (pBQ), the photophysics and photochemistry of π systems which include hetero atoms are very complex, due to the high density of electronic excited states. For further investigations on dark nπ^* states three structures were chosen:

- Xanthone (XA)
- Thioxanthone (TX)
- Acridone (AC)

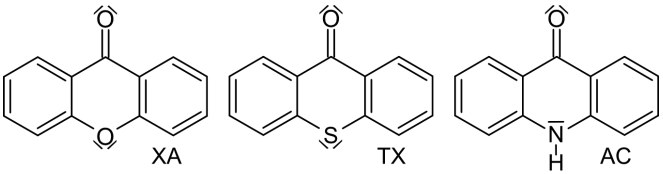

Figure 8.4.: Chemical structures of Xanthone (XA), Thioxanthone (TX) and Acridone (AC).

Xanthone and its derivatives were selected for their important role in biological systems and technical application. For example: *iso-propyl*-thioxanthone is used as a photoinitiator in printing processes, hycanthone and analogs, with its thioxanthone motif, are drugs used in chemotherapy[ARC83] and acridone is the scaffold of some synthetic compounds with various pharmacological applications[FUJ89, KEL09], mostly antiviral.

8.3.1. Xanthone

In his Ph.D. thesis in 2010 Siegert[SIE10] presented first experiments on photodetachment photoelectron spectroscopy to locate xanthone's $n\pi^*$ states. Therein, he suggested a certain order of the individual electronic states. As stated in his work, the resolution of the formerly employed PD-PE spectrometer was not fully sufficient, so only a tentative assignment could be given at that time. To further extend his works, with better resolved spectra of xanthone, different measurements with the electrostatic spectrometer, in its field-free and high resolution electron deceleration modes, were performed. Figure 8.5 displays the new spectrum taken with detachment wavelengths of 532, 355 and 266 nm. Again, the different subspectra are indicated by gray markings. Starting with the first peak on the left side of the spectrum the S_0 with a

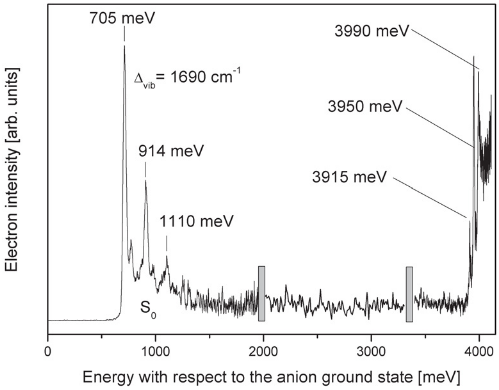

Figure 8.5.: PD-PE spectrum of xanthone. Recorded with detachment wavelengths of 532, 355 and 266 nm. S_0 and dense nπ*/$\pi\pi$* state region visible.

good resolved vibrational progression is clearly visible. The electron affinity can therefore be determined at 0.705 eV, in good agreement with former experiments and calculated data (0.69 eV). The dominant vibration of 1690 cm^{-1} can again be attributed to the C=O stretch vibration; calculated values of 1715 cm^{-1} and a proposed shortening of the C=O bond by about 3.4 percent after electron attachment support this assignment[SIE10, RAI11b] (the additionally visible low energetic vibration will be covered later). Interestingly, in the next part of the spectrum, from about 1.30 eV to 3.90 eV, neither vibrational peaks of the S_0 nor higher electronic state are visible. From the first fact, it can be stated that for the overall geometric shift in xanthone, among the neutral and the anion ground state, only minute changes are present. The unusual broad gap (3.2 eV) in between the S_0 and the higher electronic states also shows that extended π system not always correlate with low lying excited electronic states (for comparison see chapter 8.4, e.g., *trans*-stilbene with a gap of 2.18 eV). This directly conflicts with the prevalent opinion that n orbitals are spatially and energetically isolated from the bonding π and anti-bonding π^* orbitals. In fact, these orbitals are obviously influenced (blue shifted positions) by the electrostatic fields of the n electrons and their electron correlation effects. This conflict with the molecular orbitals based view, again reveals the flaws of molecular orbital diagrams, as previously mentioned in chapter 8.2. On account of the high state density in the 3.90 to 4.00 eV range, where the excited electronic states are located, higher resolution spectra of the nπ^* state region were taken. Additionally the lower frequency

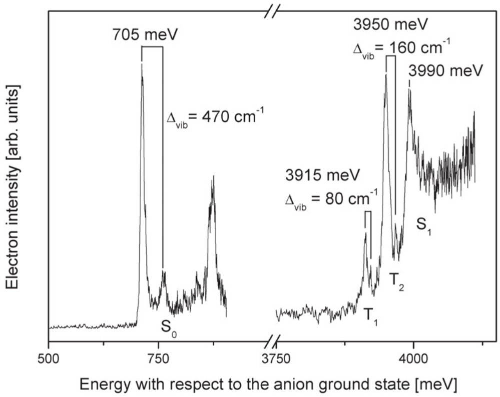

Figure 8.6.: PD-PE spectrum of xanthone with resolution enhancement through electrostatic electron deceleration. Recorded with detachment wavelengths of 532 and 266 nm. Vibrational excitations of the higher excited states are clearly visible. Peaks assigned with the help of theoretical data[RAI11b].

vibrations in the S_0 ground state were further analyzed. Again, both spectra were recorded with 532 and 266 nm but the electron velocity was reduced through the special electron optics, illustrated in chapter 7.2.2. Due to space constraints, figure 8.6 only depicts the most interesting parts of the resulting spectra from 0.55 to 1.00 eV and 3.75 to 4.15 eV. The S_0 now shows an additional vibrational peak with 470 cm^{-1} spacing. On the right side of the spectrum an upscaled version of the excited states transition range is shown. In contrast to the the former low resolution spectrum three distinct peaks are visible. State order and assignments are based on theoretical data, therefore, the first peak at 3.915 eV is attributed to the nπ^* T_1 (1^3A_2). A vibrational feature with small intensity is also detectable within 160 cm^{-1} spacing. The second, large rise (3.95 eV, vibrational peak at 80 cm^{-1}) in this region is assigned to the $\pi\pi^*$ T_2 (1^3A_1). The next transition, at 3.99 eV, presumably the nπ^* S_1 (1^1A_2), displays a broader structure with no resolved vibrations. Tentatively, this is not only attributed to vibrations of the T_2 state but also to a possible, up to now unknown, higher triplet state. As no other spectral or theoretical evidence was found for this speculative triplet state, no further assignment was performed.

The position of the optically dark nπ^* states (T_1 and S_1) just below the bright $\pi\pi^*$ states therefore facilitates the observed high ISC rates (0.97) in xanthone[SCA80]. As Siegert stated, nπ^* and $\pi\pi^*$ should differ in terms of their spectral sharpness[SIE10] as the detachment of the n orbital electron to the continuum should offer near diagonal Franck-Condon factors. Clear distinction between both states should then be possible: nπ^* states would be sharp and $\pi\pi^*$ states broad. As both nπ^* T_1 and $\pi\pi^*$ T_2 peaks are remarkably clear in appearance, the recorded spectrum does not support this assumption (for diagonal Franck-Condon factors) if assignments and state orders based on theoretical values are considered accurate. For comparison of the different calculated and experimental values of the excited states of xanthone, the compiled data is shown in table 8.1. Energies are given with respect to the neutral ground state. This work's experimental data was aligned with literature values by subtraction of the electron affinity. $\Delta E(S_0)$ and ΔE_{adia} are calculated values for vertical transition energies in vacuo at S_0 equilibrium geometry and adiabatic transitions[RAI11b]. Literature gas phase[BAB91, OHS03], optical detected magnetic resonance in crystals[CHA76] and cold liquid phase experiments in 3-methylpentane and hexane[POW71, CAV96] are given as reference data. Direct comparison of the PD-PE results with the calculated values show a good agreement within the error margins of the calculations and the experiment. As gas phase spectroscopy seems to be most accurate method, jet-cooled literature spectra of the T_1 and S_1[BAB91, OHS03] states are used to support the assignment. Surprisingly, crystal and liquid phase experiments, while often yielding shifted T_1 and T_2 positions, also roughly agree with this work's measurements. The higher electronic states (S_2, T_3, T_4),

	$\Delta E(S_0)^{[a]}$	$\Delta E_{adia}^{[b]}$	Gas phase[c]	Crystals[d]	Liqu. phase[e]	This work
Excited-state data of xanthone in eV with respect to the S_0						
S_1 nπ* 1^1A_2	3.44	3.08	3.34	3.43	3.35, 3.43	3.29
S_2 $\pi\pi$* 2^1A_1	3.88	3.62	3.64, 3.81		3.65, 3.65	?
T_1 nπ* 1^3A_2	3.26	3.12	3.20, 3.20	3.31	3.31, 3.21	3.21
T_2 $\pi\pi$* 1^3A_1	3.32	2.98		3.13, 3.15		3.24
T_3 $\pi\pi$* 2^3A_1	3.58	3.43				?
T_4 $\pi\pi$* 1^3B_1	3.66	3.55				?

Table 8.1.: Calculated (DFT/MRCI), literature and this work's experimental data of xanthone in eV. [a] calculated vertical data in vacuo[RAI11b], [b] calculated adiabatic data[RAI11b], [c] jet-cooled induced & dispersed emission[BAB91, OHS03], [d] optically detected magnetic resonance in crystal[CHA76], [e] emission spectra in 3-methylpentane (77 K)[POW71] and hexane[CAV96]

recently mentioned by Siegert in his work[SIE10, RAI11b], could not be reproduced even in the new higher resolution spectra. In conclusion, despite their well-separated lower excited electronic states and consistence with theoretical and literature data, the spectra only allow tentative assignment of the higher nπ^* and $\pi\pi^*$ states. Most importantly an additional electronic state, presumably the T_2 could be located near the T_1's position.

In a recent experimental study, Gilch and co-workers postulated an inversion of the first nπ^* and $\pi\pi^*$ states in polar solvents[HEI06]. With the location of the tightly spaced T_1 and T_2 this seems to be a rather plausible matter. As the order and solvent dependent inversions of the nπ^* and $\pi\pi^*$ states are of utmost importance for ISC processes (Scaiano, 1980[SCA80]) the herein presented findings are a valuable addition to the former studies.

8.3.2. Thioxanthone

Similar to experiments on xanthone, many studies predict an interchange of the lowest triplet and singlet, nπ^* and $\pi\pi^*$ states in liquid solutions of thioxanthone[FER06]. To clarify the state order and provide additional information, gas phase photodetachment photoelectron spectra were taken. Figure 8.7 depicts this spectrum in a condensed form, where only the interesting parts of the spectrum are shown. The spectrum was taken with detachment wavelengths of 532 and 266 nm. Although it was also recorded in the high resolution, electrostatic electron deceleration mode, no high resolution could be achieved. As the electron/ion intensities and photodetachment conditions were nearly the same as for the measurement of xanthone, this is probably caused by a molecular feature, e.g., low energy vibrations. Therefore, only $\pi\pi^*$ T_1 and nπ^* T_2 could be assigned.

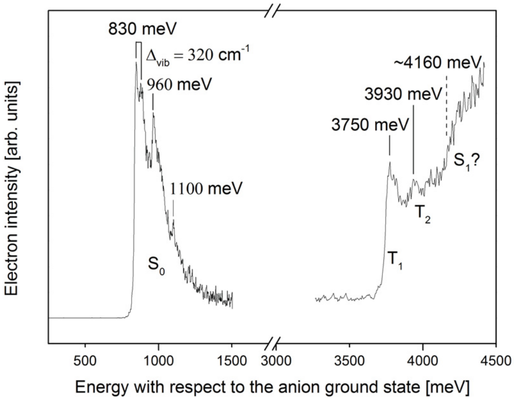

Figure 8.7.: PD-PE spectrum of thioxanthone with resolution enhancement through electrostatic electron deceleration. Recorded with detachment wavelengths of 532 and 266 nm.

The electron affinity is relatively well defined at 0.83 eV, with a small vibrational feature of 320 cm^{-1} spacing still visible in the right shoulder of the leftmost peak. This fits qualitatively to the calculated value of 0.75 eV[RAI11b]. Despite the low resolution in the higher electronic states, another, higher vibrational progression can also be seen in the S_0 with peaks at 0.96 and 1.10 eV ($\Delta E_{vib} = 1080$ cm $^{-1}$). As in the high resolution spectrum of xanthone, the medium range of the spectrum was omitted as no spectral features were present. At 3.75 eV the T_1 and at 3.93 eV the T_2 is observed. For neither of these states, higher vibrational states could be resolved. The dashed line at about 4.16 eV indicates a possible upper maximum for the nπ^* S_1 but due to the broad structure, no assignment was performed. Table 8.2 shows a list of the observed transitions, calculated and literature data. For easy comparison, all values are given in respect of the neutral ground state. Surprisingly, despite the low resolution of the spectrum, the calculated triplet energies agree well with the measured ones. On the other hand, when comparing to literature data, especially the crystal values seem to be the most accurate. The T_1 was located slightly above the literature value of 2.76 eV with an error of 0.16 eV; the T_2, despite being a hard-to-locate nπ* transition, even with only an error of 0.03 eV.

	$\Delta E(S_0)$[a]	ΔE_{adia}[b]	Liqu. phase[c]	Crystals[d]	This work
Excited-state data of thioxanthone in eV with respect to the S_0					
S_1 nπ* 1^1A_2	3.37	3.00	3.29		≤3.33
S_2 $\pi\pi$* 2^1A_1	3.44	3.34	3.43	3.10	
T_1 $\pi\pi$* 1^3A_1	2.96	2.81		2.76	2.92
T_2 nπ* 1^3A_2	3.20	2.88		3.07	3.10
T_3 $\pi\pi$* 2^3A_1	3.49	3.34			
T_4 $\pi\pi$* 1^3B_2	3.52	3.45			

Table 8.2.: Calculated (DFT/MRCI), literature and this work's experimental data of thioxanthone in eV. [a] calculated vertical data in vacuo[RAI10], [b] calculated adiabatic data[RAI11a], [c] liquid phase data in cyclohexane[BUR91], [d] ODMR and phosphorescence data in neat crystals[SUG81]

To be able to give a clear and scientifically sound interpretation of the recorded spectra further experimental and theoretical studies will be needed to fully assign the visible peaks in the spectrum.

8.3.3. Acridone

For acridone, the PD-PE spectrum was surprisingly clear in spite of its unstable anion beam and easy degradation of the sample due to thermal decomposition in the nozzle. In figure 8.8 three distinct electronic states are visible. Again, the leftmost peak is attributed to the anion to neutral ground state (S_0) transition and defines the electron affinity. The S_0 is, therefore, located at 0.56 eV (in respect of the anion ground

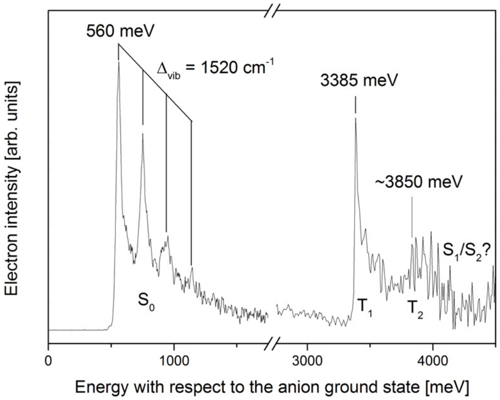

Figure 8.8.: PD-PE spectrum of acridone recorded with detachment wavelengths of 532 and 266 nm.

state) with a clear vibrational feature at 1520 cm^{-1} spacing. This progression may be caused by the C=O stretch vibration at 1655 cm^{-1} (theoretical calculation)[RAI11b]. In comparison to the calculated value of $EA_{(calc)} = 0.46$ meV[RAI11b], the measured electron affinity is in relatively good agreement. Similar to the high resolution xanthone and thioxanthone spectra the middle part of the spectrum was omitted as no spectral information, beside a baseline, could be obtained from this part. The next visible electronic state is the T_1 at 3.39 eV. It is astonishingly sharp and well separated from the T_2. In contrast to this the T_2 at about 3.85 eV is rather broad so only a maximum energy for its origin is given. It should be noted that, although table 8.3 seems to convey a semblance of an unexplored scientific field, many experiments were performed on substituted acridones. As acridone derivatives were not in the focus of this work, their results will not be covered here.

	$\Delta E(S_0)^{[a]}$	Gas. phase[b]	This work
Excited-state data of acridone in eV with respect to the S_0			
S_1 $n\pi^*$	3.46		?
S_2 $\pi\pi^*$	3.50	3.38	?
T_1 $\pi\pi^*$	2.94		2.83
T_2 $n\pi^*$	3.30		$\leq$3.29
T_3 $\pi\pi^*$	3.58		
T_4 $\pi\pi^*$	3.58		

Table 8.3.: Calculated (DFT/MRCI), literature and this work's experimental data of acridone in eV. [a] calculated vertical data in vacuo[RAI10], [b] gas phase fluorescence excitation[MIT00].

When compared, both measured values are in good agreement with the calculated data[RAI11b, MIT00]. Therefore, an assignment of T_1 and T_2 seems plausible. For the S_1 and S_2 states no peaks are observed which could be mainly caused by the low signal-to-noise ratio and the earlier mentioned unstable anion signal. Additionally, one of the main differences from the spectra of xanthone and thioxanthone, no broad high intensity electron signal was observed in the range between 3.50 and 4.5 eV. As only a tentative proposition of an additional forbidden electronic state was given for xanthone/thioxanthone, so far no further explanation for the missing spectral features exists.

8.4. Carotene analogs[VS11]

As reviewed in many textbooks, long aromatic polyenes (the so called carotenes) often play an important role in biological systems. Their huge π systems display low-lying electronic states and therefore shift the respective absorptions into the visible range of the electromagnetic spectrum. From there the energy is stored in long lived molecular states by radiation-less interconversion to dark electronic states. For example, in photosynthesis light is transformed into chemical energy, which is then used to transform carbon dioxide into organic compounds (most prominently oxygen and different sugars). The radiation is absorbed by antenna chlorophyll complexes in the thylakoid membranes of the chloroplasts. The light-harvesting complexes (LHC) aids the absorption of light by channeling photon energy into the reactive center chlorophyll (also known as special pair), where a charge separation is created which leads to an electronic current. These light harvesting complexes consist of chlorophyll (porphyrin derivatives), carotenes and oxacarotenes (xanthophylls)[NEL05]. Due to carotenes' transition forbidden S_1 and short-lived S_2 state, their role and functionality is still not fully understood. It is assumed that they act as a triplet quencher due to their presumably low-lying T_1 states. In addition they are known to eliminate radicals and other reactive species. To understand their electronic state energetics, dark states of short carotene analogs were investigated. To mimic some of these special complexes, the α, ω-diphenylpolyenes *trans*-stilbene (SB), all-*trans*-1,4-diphenyl-1,3-butadiene (DPB) and all-*trans*-1,6-diphenyl-1,3,5-hexatriene (DPH) were chosen[VS11]. See Figure 8.9 for their respective chemical structures. The herein presented and reproduced findings were also covered in a publication in 2011[VS11]. All presented spectra were recorded with the magnetic bottle spectrometer.

In longer polyenes the S_1 (2^1A_g) state's wave function is dominated by a special doubly excited electron configuration were the HOMO is fully depopulated (two holes) and the two respective electrons reside both in the LUMO (H^{-2}, L^{+2}). The first single excited configuration (H^{-1}, L^{+1}) is then the S_2 (^1B_u).

As a specialty in SB, DPB and DPH the energetic order of the transition-forbidden 2^1A_g and the fully allowed ^1B_u interchange with increasing chainlength[ALL89]. Earlier gas phase studies located the 2^1A_g above

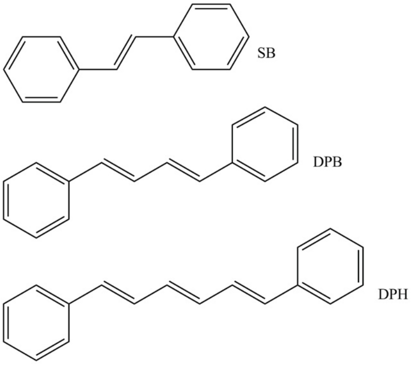

Figure 8.9.: Chemical structures of the α,ω-diphenylpolyenes *trans*-stilbene (SB), all-*trans*-1,4-diphenyl-1,3-butadiene (DPB) and all-*trans*-1,6-diphenyl-1,3,5-hexatriene (DPH).

the S_1 (1^1B_u) at 3.997 eV in SB[SYA82, AMI83, MAJ84], in DPB 0.033 eV below the 1^1B_u (3.706 eV)[SHE83, HEI83] and finally in DPH about 0.420 eV below the 1^1B_u (3.615 eV[KOH84]). SB, as the smallest of the three investigated polyenes, displays a remarkable photoinduced *cis-trans* isomerization via excited singlet states[SAL94, MOL97, SAL98, SAL00, GAG02] [QUE03, MIZ09, WEI10]. For the longer polyenes, DPB and DHP, *cis-trans* isomerizations also exist but with much lower efficiencies[ALL89]. To discuss intensities and electronic selection for radical anion PD-PES, the electronic states of DPH, including their leading molecular orbital configurations, are shown in Figure 8.10. Some electronic states (e.g., S_0, T_1 and the 1^1B_u S_2) are dominated by a single electron configuration. For the T_2 and 2^1A_g S_1 states the wavefunction consists of a linear combination of different single and multiple excited electronic configurations. The OPOE rule states that one photon only interacts with one electron (see page 13 for explanation). So simultaneous photoexcitation and photodetachment processes are very unlikely. Therefore, the tran-

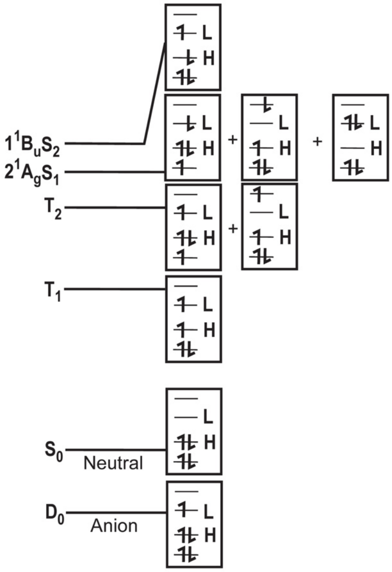

Figure 8.10.: Electronic state scheme of DPH including the leading molecular orbital configurations[VS11]. Note the contribution of doubly excited states, which cannot be reached by one photon one electron excitations.

sition intensities in PD-PES should mainly be governed by the sum of the squared contributions of single-hole configurations (SCSHC). Calculated SCSHC values for SB, DPB and DPH are given in Table 8.4. For example for the T_2 state of DPH, the left configuration (SCSHC of 0.42 $(\text{H-1})^{-1}$) mainly influences the PD-PES intensity, as only this configuration can be reached by removal of one electron from the anion. The right configuration would require electron removal and simultaneous excitation $(\text{LUMO+1})^{+1}$ which is not possible due to the OPOE selection rule.

8.4.1. Results

To be able to give a comprehensive description of the measured data this section will cover some of the theoretical results first and then examine and discuss the individual spectra in separate subsections.

Literature data shows no evidence of single cis or mixed cis and trans conformers in gas phase experiments[SYA82, AMI83, HEI83, SHE83, KOH84] [MAJ84]. Therefore, it is also plausible to assume all-*trans* configurations for the DPB and DPH measurements presented in this work. Experimental electron affinities were determined for SB, DPB and DPH by using the upper left edge of the D_0 to S_0 (anion to neutral ground state) transition. Measured EA values are presented in Table 8.5 and compared to theoretical data (DFT, B3LYP). As anticipated the electron affinities develop proportionally to the respective molecules length and size of the π system. The calculated adiabatic EAs are in remarkably good accordance to the experimental values. The differences are about 50 meV in SB (exp.: 0.39 eV, calc.: 0.34 eV), 20 meV in DPB (exp.: 0.67 eV, calc.: 0.69 eV) and 80 meV in DPH (exp.: 0.89 eV, calc.: 0.97 eV). As figure 8.11 shows, the calculated values, despite being in an overall agreement with the measured ones, display a steeper rise in respect of the molecules size. This indicates that for longer π systems the calculations are increasingly inaccurate. Overestimating the electron affinities, is a trend also found in α-oligothiophene chains of monomer units ranging from two to six[SV11b]. Normally, quantum chemical calculations would underestimate the effects of electron correlation and should therefore also underestimate the stability of the anion with respect to the neutral molecules simply because the anion has one additional electron in contrast to the neutral molecule. Thus, the resulting calculated EAs are expected to be to low in comparison to the experimentally determined values. As this effect is neither understood

	ΔE(S_0)[f(r)]	ΔE$_{adia}$	ΔE(D_0)	hole conf.	literature data	exp. data
Excited-state data of SB						
S_1 1^1B_u	4.00 [0.86]	3.72	3.62	0.86 (H)$^{-1}$	theo: 4.591[a], exp: 3.997[b]	?
S_2 2^1A_g	4.20	(3.82)	3.94	0.40 (H-2)$^{-1}$	theo: 4.894[a]	
S_3 2^1B_u	4.23 [0.26]		3.94	0.40 (H-1)$^{-1}$		
T_1 1^3B_u	2.54	2.01	2.05	0.85 (H)$^{-1}$	2.128[c]	2.18
T_2 1^3A_g	3.70	3.56	3.51	0.38 (H-3)$^{-1}$		3.60
T_3 2^3B_u	3.97		3.79	0.44 (H-1)$^{-1}$		
T_4 2^3A_g	4.02		3.83	0.38 (H-2)$^{-1}$		
Excited-state data of DPB						
S_1 2^1A_g	4.00	(3.44)	3.44	0.19 (H-1)$^{-1}$	theo: 4.154[a], exp: 3.673[d]	?
S_2 1^1B_u	3.64 [1.67]	(3.39)	3.27	0.90 (H)$^{-1}$	theo: 4.246[a], exp: 3.706[d]	?
S_3 2^1B_u	4.04 [0.04]		3.74	0.36 (H-2)$^{-1}$		
S_4 3^1A_g	4.10		3.74	0.35 (H-3)$^{-1}$		
T_1 1^3B_u	2.11	1.68	1.64	0.83 (H)$^{-1}$	1.788[e]	1.82
T_2 1^3A_g	3.24	3.11	3.04	0.42 (H-1)$^{-1}$		3.26
T_3 2^3B_u	3.85		3.67	0.41 (H-2)$^{-1}$		
T_4 2^3A_g	3.87		3.69	0.41 (H-3)$^{-1}$		
Excited-state data of DPH						
S_1 2^1A_g	3.49	(2.88)	2.86	0.18 (H-1)$^{-1}$	theo: 3.537[a], exp: 3.192[f]	?
S_2 1^1B_u	3.31 [2.20]	3.07	2.96	0.88 (H)$^{-1}$	theo: 3.902[a], exp: 3.615[f], 3.22[g]	?
S_3 3^1A_g	3.91		3.61	0.30 (H-3)$^{-1}$		
S_4 2^1B_u	3.92 [0.02]		3.61	0.30 (H-2)$^{-1}$		
S_5 3^1B_u	4.46 [0.01]		3.89	0.23 (H-4)$^{-1}$		
T_1 1^3B_u	1.80	1.40	1.35	0.81 (H)$^{-1}$	1.49[h], 1.53[i]	1.54
T_2 1^3A_g	2.84	2.71	2.64	0.42 (H-1)$^{-1}$		2.94
T_3 2^3B_u	3.65		3.51	0.25 (H-2)$^{-1}$		
T_4 2^3A_g	3.78		3.61	0.36 (H-3)$^{-1}$		
T_5 3^3B_u	3.80		3.64	0.25 (H-2)$^{-1}$ 0.11 (H-4^{-}1		

Table 8.4.: Experimental, calculated (DFT/MRCI) and literature data of SB, DPB, DPH in eV from [VS11]. [a]Vertical values at S_0 geometry (CAS-CI MRMP)[MIZ09], [b]jet-cooled gas phase[SYA82], [c]phosphorescence in crystals, 4.2 K[IKE85, IKE94], [d]fluorescence in He jet[SHE83], [e]orthorhombic DPB crystals[TEK94], [f]fluorescence in He jet[KOH84], [g]one-photon absorption in EPA matrix, 77 K[FAN78], [h]monoclinic DPH crystals[WEI92], [i]orthorhombic DPH crystals[WEI92].

	SB	DPB	DPH
EA_{calc}	0.34	0.69	0.97
EA_{exp}	0.39	0.67	0.89

Table 8.5.: Experimental and calculated (DFT, B3LYP) electron affinities of SB, DPB, DPH in electron volts[VS11].

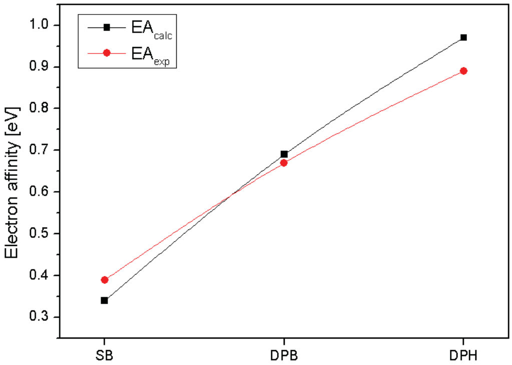

Figure 8.11.: Comparison of the different experimental and calculated electron affinities vs the molecule size.

nor corrected by additional calculatory parameters, this clearly shows the need for reliable experimental methods to give valuable comparison spectra for calibration and directly justifies the effort for complex methods like PD-PE spectroscopy.

Stilbene

The PD-PE spectrum of SB (fig.: 8.12 composed from three spectra recorded with wavelengths of 1064, 355 and 266 nm to optimize the PE resolution for each part of the spectrum with a resulting overall resolution of 30 meV. The clean baseline before the S_0 onset reveals

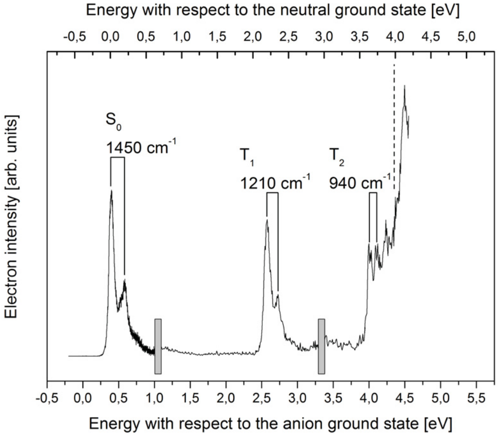

Figure 8.12.: PD-PE spectrum of SB composed of three spectra[VS11] recorded with wavelength of 1064, 355 and 266 nm to optimize the PE resolution for each part of the spectrum. Displayed are the S_0, T_1 and T_2 states. T_2 location is based on theor. calculations. The steep rise to the right of the spectrum is assigned to a overlapping of different electronic states. The dotted line denotes the position of the 1^1B_u from gas phase literature.

no existence of hot-band contribution to the spectrum. Therefore it is assumed that the molecules are sufficiently cooled upon expansion and subsequently after electron attachment. The neutral S_0 ground state is situated at about 0.39 meV over the anion ground state. A vibrational feature of 1450 cm^{-1} is clearly resolved in the first electronic state. 2.19 eV above, the first triplet state T_1 can be located with a vibration spacing of 1210 cm^{-1}. This value agrees well with calculated (2.01 eV) and slightly red-shifted literature date from crystal experiments (2.128 eV[IKE85, IKE94]). Calculated values predicted the T_2 to lie adiabatically at 3.56 eV, well below the S_2 state at about 3.83 eV[SYA82]. Therefore the rise in signal at 3.60 eV is attributed to the T_2 state. SCSHC values of $S_0 = 0.86$, $T_1 = 0.85$ and $T_2 = 0.38$ support this assignment by comparison with the received intensities in the spectrum. A somewhat smaller vibrational spacing of 940 cm^{-1} also hints towards an assignment to the T_2. The literature data position of the S_1 is marked by a dotted line in the spectrum and situates the S_1 right below the broad rise of the overlapping higher electronic states. Computed data (3.72 eV) also states this range as a proper location of the S_1. In the spectrum a peak is visible at this position but unfortunately not intense enough to justify a clear assignment. According to calculations the strong rise at 4.15 eV is based on overlapping electronic states composed of higher S_1 vibrations, S_2, T_3 and T_4.

1,4-diphenylbutadiene

Subspectra for DPB were recorded with wavelengths 1064, 355, 266 and 212.7 nm. The resulting combined spectrum is shown in figure 8.13. Isolated S_0 and T_1 peaks are clearly visible. Similar to SB, each peak displays vibrational information, although of smaller spacing in S_0 (1370 cm^{-1}) and larger spacing in T_1 (1290 cm^{-1}). Interestingly the intensities of the vibrational progression in T_1 does not conform to normal Franck-Condon induced vibrational patterns. This is mainly attributed to anionic resonances as explained in subsection 7.2.2. The position of the T_1 (1.82) is in good agreement with solid-state crystal literature (1.788 eV)[TEK94] and calculated adiabatic values(1.68 eV). In contrast to SB the T_2 transition at 3.26 eV is clearly distinguishable from other higher electronic states. Its assignment is based on former gas phase S_1 data[SHE83] and comparison of the theoretical T_2 (3.11 eV) and S_1 (3.39 eV) state energies. Additional justification is gained

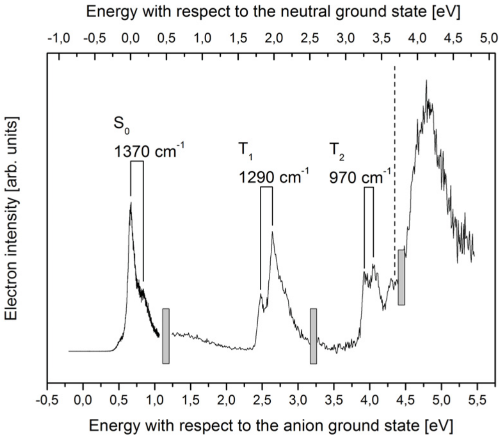

Figure 8.13.: PD-PE spectrum of DPB[VS11] composed of four spectra recorded with wavelength of 1064, 355, 266 and 212.7 nm. Modulation of the T_1 state is caused by anionic resonances. T_2 location can now clearly be distinguished from the overlapping electronic states to the right. The dotted line denotes the position of the 1^1B_u from gas phase literature.

by observation of the predicted intensity ratio of 2:1 between the T_1 (SCSHC = 0.83) and T_2 (SCSHC = 0.42) states. A small (but slightly larger than in SB) vibrational spacing of 970 cm^{-1} is observed. At about 3.60 eV a distinct peak of similar intensity arises, which is tentatively attributed to the 2^1A_g S_1 and 1^1B_u S_2 states, as both states should overlap ($\Delta E = 267$ cm^{-1})[SHE83] at about 3.67 eV in the spectrum. SCSHC values corroborate this statement as in DPB the bright S_2 (SCSHC = 0.90) should heavily interfere with the only barely visible S_1 (SCSHC = 0.19). Again, the rest of the spectrum is dominated by a broad, intense transition of overlapping higher electronic states.

1,6-diphenylhexatriene

For DPH the PD-PE subspectra were recorded with wavelengths of 1064, 355, 266 and 212.7 nm. The first thing to note is the small unresolved structure before the S_0 state (marked by •) which is mainly attributed to a thermally induced pericyclic reaction's product. Different possible types of products are discussed in reference [ALL89]. T_1 state energy was determined to be 1.54 eV, in good accordance to solid-state crystal of monoclinic (1.499 eV) and orthorhombic (1.526 eV) elementary cells[WEI92]. A theoretical adiabatic value was calculated with 1.40 eV. Again, anion excited states modulate the Franck-Condon factors of

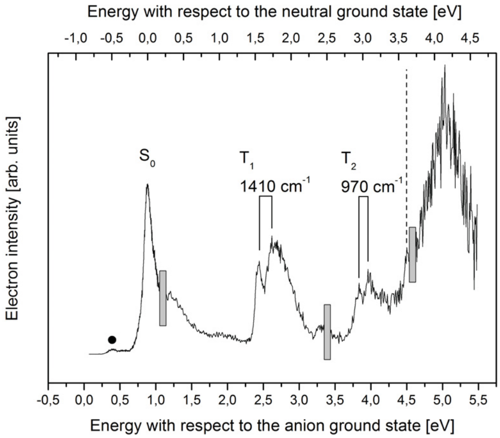

Figure 8.14.: PD-PE spectrum of DPH[VS11] composed of four spectra recorded with wavelength of 1064, 355, 266 and 212.7 nm. Modulations of the T_1 & T_2 states are caused by anionic resonances. The predicted 2^1A_g (S_1) state is not clearly visible. The dotted line denotes the position of the 1^1B_u (S_2) from gas phase literature.

the different vibrational peaks (1410 cm^{-1} spacing), leading to a broad spectral structure. The T_2 (2.94 eV) is clearly offset from the higher electronic states. Assignment was performed with the help of theoretical calculations (2.71 eV). Again the intensities are in good agreement with the calculated SCSHC values ($T_1 = 0.81$, $T_2 = 0.42$). All trends in both vibrational coutures are conforming with findings in SB and DPB except for the very small change between the DPB and DPH T_2 vibrational spacing (both 970 cm^{-1}, resolution limited).
SCSHC calculations predict very weak 2^1A_g S_1 state intensities (SCSHC = 0.18), which therefore cannot be detected in the PD-PE spectrum. Calculations estimate a location at about 2.88 eV, which are backed up by two-photon absorption experiments in EPA (solvent consisting of mixed ether, pentane and alcohol) at 77 K (3.12 eV)[FAN78] and gas phase data (3.19 eV)[KOH84]. Gas phase literature on the 1^1B_u S_2 is marked with a dotted line at 3.62 eV[KOH84]. Theoretical calculations and other solid state experiments located this state at 3.07 and 3.22 eV (in EPA, 77 K)[FAN78]. In this work's spectrum no evidence can be found due to laser-background induced limitations. Again, the rest of the spectrum is dominated by a broad, intense transition of overlapping higher electronic states (T_3, T_4, S_3, S_4) within an energy range of 0.38 eV.

8.4.2. Discussion

Similar to former findings in oligothiophenes[SV11b] the T_2 state is situated below the S_1. In addition to the classical relaxation from S_1 to T_1 this provides another possible ISC pathway to the T_2 state. As the S_1-T_1 energy difference is large, the ISC rates for this energetic channel are rather low[ENG70]. Therefore the S_1-T_2 relaxation becomes the dominant ISC pathway. However, as α,ω-diphenylpolyenes do not possess heavy heteroatoms, ISC rates are by a number of magnitudes smaller[BEN76, GRO79, SAL00] than in oligothiophenes[SV11b]. Recent findings by Marian and co-workers[KUE11] indicate another possible aspect. In DPH the spin-orbit coupling (SOC) between the symmetry-forbidden (planar conformation) 1^3A_g T_2 and 1^1B_u S_2 states increases drastically with torsional deformations on the central bond. Additionally, along this reactive axis, the corresponding potential energy surfaces intersect. When compared to the 1^3A_g T_2 and 2^1A_g S_1 states, the spin-orbit coupling of the latter states is rather small, caused mainly by their similar electron configuration (see figure 8.10 for reference). Combining both facts allows to speculate on a potential relaxation pathway via excited triplet states in DPH. In the first step energy from an optical excited molecule in the 1^1B_u S_2 is transferred to the long-lived[ITO87, ITO07] 2^1A_g S_1 state. From there the S_1 and S_2 states can now efficiently convert population by electronic state coupling and thermal re-population as found by Hilinski et al.[HIL96]. Marian and co-workers predict that instead of the low yield 2^1A_g S_1 to 1^3B_u T_1 ISC process, ISC to the 1^3A_g T_2 state mainly occurs from the higher 1^3A_g S_2. From there it is now possible to relax into the 1^3B_u T_1 by internal conversion and subsequent vibrational relaxation into its vibrational ground state[KUE11]. Once the T_1 is populated, isomerization processes via the triplet pathway are possible. In some special solvents the yields of this mechanism can even compete with the classical singlet isomerization channel as shown by Saltiel et al.[SAL00]. As an explanation, Marian and co-workers state the flat 1^3B_u T_1 potential surface along the torsional coordinate thus predicting a very high isomerization probability in T_1 on population.

For the other α,ω-diphenylpolyenes SB and DPB, ISC is negligibly small and therefore of minor importance.

8.5. Azulene

Azulene, an aromatic hydrocarbon composed of a five- and a seven-membered ring, is well known for its unique light emission properties. Early experimental studies in glassy EPA by Beer and Longuet-Higgins in 1955 showed a peculiar fluorescence pattern with a supposed large separation (about 1.80 eV) of the two lowest electronic singlet states[BEE55]. One year later Viswanath and Kasha conducted similar experiments and assigned the anomalous fluorescence to the $S_2 \rightarrow S_0$ transition[VIS56], with azulene being the first observed molecule to violate Kasha's rule[KAS50]. In none of the studies phosphorescence from the lowest triplet state could be detected. Nevertheless, Kasha and co-workers gave a tentative explanation for the missing $S_1 \rightarrow S_0$ fluorescence by the prediction of 'an excited triplet' [...] 'at nearly the same energy as the S_1 level'[VIS56]. This hypothesis was deemed to be rather unlikely by them, due to the interpretation 'that [all] light absorbed in the visible absorption band would be converted completely to lowest triplet state excitation'[VIS56]. Nevertheless, as the experiments on xanthone earlier showed, ISC rates up to 0.97[SCA80] have been observed and therefore, the triplet state relaxation dynamics seemed to be a possible scenario. To confirm the location of the presumably photophysically important T_1 state, photodetachment photoelectron experiments were conducted during this work.

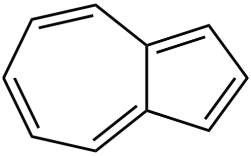

Figure 8.15.: Chemical structure of azulene.

Figure 8.15 shows the PD-PE spectrum of azulene recorded with detachment wavelengths of 1064, 532, 355 and 266 nm. The joints of each subspectrum are displayed by grey markings. The different electronic states are labeled with their respective transition energy with respect to the anion ground state. For easy comparison with the literature and calculated values, the measured electron affinity was subtracted and an additional scale, in respect of the neutral ground state, added on top of the spectrum. The position of the literature gas phase value for the S_1 state[SUZ87] is indicated by a dashed line. The leftmost electronic states is the S_0 at 0.79 eV (with respect to the anion ground state D_0), with a vibrational progression at about 610 cm^{-1} spacing. This is good agreement with the literature value of EA = 0.79±0.0080 eV

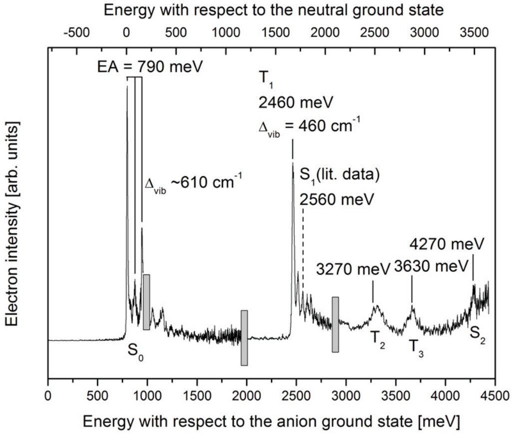

Figure 8.16.: PD-PE spectrum of azulene. The PD-PES were recorded with 1064, 532, 355 and 266 nm; joints are indicated by gray marking. Literature position[SUZ87] of the S_1 state marked by dashed line.

by Schiedt et al.[SCH00]. At 2.46 eV the first excited electronic state is visible (vibrational features: 460 cm^{-1}). An additional peak at about 1.94 eV, formerly measured by Knott et al.[KNO98] in a similar experiment and later mentioned by Boesl et al.[BOE98]in a review article, could not be reproduced. In comparison with the calculations and the literature data (for references see below), it is therefore expected that two states, namely T$_1$ and S$_1$, should reside in this region (around 2.46 eV) of the spectrum. The next two peaks, at 3.27 and 3.63 eV, feature a broad structure, which seems to be caused by an unresolved vibrational structure. They are attributed to the T$_2$ and T$_3$ states. The last visible peak is the (fluorescent) S$_2$ at 4.27 eV, which is only barely visible due to the rising one-photon background in this spectral range. Table 8.5 gives an overview over the different experimental and theoretical[MAR11] values in comparison to literature data. Many previous studies, which

	ΔE(S$_0$)[a]	Gas phase[b]	Crystals[c]	Liqu. phase[d]	This work
Excited-state data of azulene in eV with respect to the S$_0$					
S$_1$	2.19	1.77[SUZ87]			(1.77)
S$_2$		3.56[SEM09]	3.32[VIS56]		3.48
T$_1$	2.01		1.72[KLE83]	1.69[HER75]	1.67
T$_2$	2.46				2.48
T$_3$	2.75				2.84

Table 8.6.: Calculated, literature and this work's experimental data of azulene in eV. [a] calculated vertical data in vacuo[MAR11], [b] jet-cooled, gas phase spectroscopy[SUZ87, SEM09], [c] crystal data in EPA at 77 K[VIS56] and phenazine at 30 K[KLE83],[d] liquid phase flash photolysis[HER75]

tried to locate the lowest electronic state states, used many different methods. Therefore, from the many citations, crystal data and the more accurate jet-cooled gas phase spectroscopy values were chosen for comparison. As a first noteworthy fact it can clearly be seen that the literature S$_1$ value (1.77 eV[SUZ87]) does not fully agree with to the first rise in the spectrum at 1.67. The often cited T_1 state energy, located at 1.30 eV by Rentzepis[REN69] could not be reproduced. Already in 1975, Herkstroeter published doubts about this location[HER75]. Therefore, the formerly stated possibilities of S_1 being the first excited state or an extremely low triplet state were dismissed. As the intensities of the peaks (now assigned to the S_1) do not follow the exponential Franck-Condon progression of the alleged origin, the peak at 1.67 eV was assigned to the T_1 state. This is in surprisingly good agreement with data obtained in phenazine crystals at 30 K[KLE83] and liquid phase flash photolysis[HER75]. Normally, liquid and solid phase tend to differ from gas phase experiments due to environmental effects. To be absolutely sure about the position and to rule out all possible anion excited state effects in this works spectrum, the measurements will be repeated with additional, different wavelengths currently not available.

Calculated values for T_1 and S_1 at 2.01 and 2.19 eV (each with inversed dipole direction)[MAR11] are positioned slightly to high but at least support the electronic order. The offset in the calculations can easily be explained by the fact that only vertical and no adiabatic values are given, which shifts the position to higher energies in cases of geometrical differences. Nevertheless, the newly found T_2 and T_3 (2.48 and 2.84 eV) positions are in good agreement with the calculated values of 2.46 and 2.75 eV[MAR11]. The S_2, first mentioned by Kasha and co-workers (3.32 eV[VIS56]) and recently remeasured with ‘rotationally resolved ultrahigh-resolution laser spectroscopy’ (3,56 eV[SEM09]) could also be located with high probability in near the literature values.

9. Conclusion and outlook

The goal of this work was to perform optical spectroscopy of photophysically and photochemically important electronic states, such as triplet, nπ* and electric dipole forbidden states. In the course of this work, many of this so-called ‘forbidden transition’ were located and assigned. As the name ‘forbidden states’ may imply an absolutely impossible transition, it was found early that for many of these states it is nevertheless possible to excite them. For their extremely low intensities in classical optical spectroscopy, this work now suggests to use the term ‘dark states’ for these special electronic states.

The main focus of the experimental work was based on the technical advancement of the spectrometer and the upgrading of the old low-resolution magnetic bottle system with a combined electrostatic and field-free time-of-flight electron spectrometer. Therefore, three major improvements had to be made: the incorporation of the new spectrometer system, the possibility to perform temporal and spatial adjustment and last but not least the implementation of the high-resolution electron deceleration setup. For both of the two latter improvements the development of the movable electron optics was the key to success. It is therefore now possible to quickly select between high-transmission or high-resolution, resulting in three distinct modes of operation of the photodetachment photoelectron spectrometer:

- Low-resolution (ΔE of 25 to 40 meV), high-transmission magnetic bottle PS-PES; for overview spectra, to quickly locate interesting regions for electronic transitions and identify anion excited states
- Medium-resolution (ΔE of 10 meV), selectable transmission field-free PES; for easy adjustment of the mass spectrometer and the laser system

- High-resolution (ΔE of 2.6 meV), low transmission electrostatic PES; decelerated electrons allow the use of nearly arbitrary wavelengths, to avoid anion excited and autodetachment states, while still maintaining the high resolution of low energetic electrons

Additionally, for better sample preparation and higher masses the inlet system with its nozzle was upgraded. With the high-temperature ceramic inlays to avoid sample decomposition and the thermal insulation from the rest of the system it is now possible to achieve vaporisation temperatures up to 590 K.

Despite the high complexity of the spectrometer an the various difficulties in its construction, several different biologically and photophysically interesting sample molecules were analyzed. While the first attempts on *p*-benzochinone mainly yielded a validation of the method's fitness for measuring nπ* states[SV11a], PD-PE spectra of xanthone already showed nearly perfect information on the location of the first triplets T_1 and T_2. For the xanthone analogs thioxanthone and acridone promising data towards T_1 was also found. Electron affinities for all molecules were obtained and could be proven by comparison with calculated values[RAI11b, SV11a].

For a number of aromatic hydrocarbons the lowest electronic states, including the anion-to-neutral transition, could also be located. In the α,ω-diphenylpolyenes a possible explanation for the T_2 and its non-involvement in the ISC processes could be given[VS11]. In particular the energetic position of T_1 below the S_1 in azulene could be proven, a presumption already made, but never proven, by Kasha in 1956[VIS56].

Still, some problems remain with the current setup. For a huge number of molecules the resolution is now fair enough to be able to discriminate the different electronic in the spectra. However, for some special cases where the spacings between the peak are too small (see chapter

8.2) additional resolution enhancement is required. In the later course of this work it was found that the main problem now is a coulombic repulsion of the electron's space charge in the anion cloud. To solve this problem, it will be necessary to reduce either the anion count or the anion cloud's density. As lower anion counts would massively prolong recording times, a collinear laser access will be incorporated for improvement of the resolution. For further enhancement, a new commercially available 500 ps pulse length laser system, based on the current setup, will also be adapted for photodetachment. On the other hand, experiments on acridone and *1,8*-diphenyloctatetraene (not shown in this work) revealed the need for a new system for thermally unstable and non-volatile samples. Especially for *1,8*-diphenyloctatetraene only a cyclization's product could be observed. Therefore, a new laser desorption vaporization source is being developed at the moment.

As a concluding remark it can be stated that photoelectron photodetachment spectroscopy is a well-suited method to obtain important information about electronic excited states. This information helps to elucidate new pathways in photophysical and photochemical processes of many chemical substances.

10. Bibliography

[ALL39] J.S. Allan, *The Detection of Single Positive Ions, Electrons and Photons by a Secondary Electron Multiplier*, Phys Rev. **55**, 966-971 (1939)

[ALL47] J.S. Allan, *An Improved Electron Multiplier Particle Counter*, Rev. Sci. Instrum. **18**, 739-750 (1947)

[ALL84] M. Allan, Chem. Phys. **84**, 311-319 (1984)

[ALL89] M.T. Allen and D.G. Whitten, Chem. Rev. **89**, 1691-1702 (1989)

[AMI83] A. Amirav and J. Jortner, Chem. Phys. Lett. **85**, 295-300 (1983)

[ARC83] S. Archer, A.H. Zayed, R. Rej and T.A. Rugino, J. Med. Chem. **26**, 1240-1246 (1983)

[ASB79] L. Åsbrink, G. Bieri, C. Fridh, E. Lindholm and D.P. Chong, Chem. Phys. **43**, 189-185 (1979)

[ATK97] P.W. Atkins, *Physical Chemistry, Third Edition*, (1997)

[BAB91] M. Baba, T. Kamei, M. Kiritani, S. Yamauchi and N. Hirota, Chem. Phys. Lett.**185**, 354-358 (1991)

[BAE06] M. Baer, *Beyond Born-Oppenheimer: Electronic Nonadiabatic Coupling Terms and Conical Intersections*, John Wiley and Sons, London (2006)

[BAR75] J.A. Barltrop and J.D. Coyle, *Excited states in organic chemistry*, John Wiley and Sons, London (1975)

[BEE55] M. Beer and H.C. Longuet-Higgins, J Chem. Phys. **23**, 1390-1391 (1955)

[BEN76] R. Bensasson, E.J. Land, J. Lafferty, R.S. Sinclair and T.G. Truscott, Chem. Phys. Lett. **41**, 333-335 (1976)

[BOE92] U. Boesl, R. Weinkauf and E.W. Schlag, Int. J. Mass Spectrom. Ion Processes **112**, 121-166 (1992)

[BOE98] U. Boesl and W.J. Knott, Mass Spectrom. Rev. **17**, 275-305 (1998)

[BOT00] A.R. Bottril, Ph.D. Thesis, *High-energy Collision-induced Dissociation of Macromolecules using Tandem Double-focusing/Time-of-flight Mass Spectrometry*, Warwick University (2000)

[BRO56] K.L. Brown and G.W. Trautfest, *Faraday-Cup Monitors for High-Energy Electron Beams*, Rev. Sci. Instrum. **27**, 696-702 (1956)

[BRO81] J.A. Browder, R.L. Miller, W.A. Thomas and G. Sanzone, Int. J. Mass Spectrom. Ion Phys. **37**, 99-108 (1981)

[BRU67] C. Brunné, Z. f. Naturforsch. **22b**, 121-123 (1967)

[BRU72] C.R. Brundle, M.B. Robin and N.A. Kuebler, J. Am. Chem. Soc. **44**, 1466-1475 (1972)

[BUR91] D. Burget and P. Jacques, J. Chim. Phys. **88**, 675-688 (1991)

[CAV96] J.J. Cavaleri, K. Prater and R.M. Bowman , Chem. Phys. Lett. **259**, 495-502 (1996)

[CED77] L.S. Cederbaum and W. Domcke, Adv. Chem. Phys. , 205-344 (1977)

[CHA76] A. Chakrabarti and N. Hirota, J. Phys. Chem. **80**, 2966-2972 (1976)

[CHE87] O. Cheshnovsky, S.H. Yang, C.L. Pettiette, M.J. Craycraft, and R.E. Smalley, Rev. Sci. Instrum. **58**, 2131-2138 (1987)

[COO75] C.D. Cooper, W.T. Naff and R.N. Compton, J. Chem. Phys. **63**, 2752-2757 (1975)

[DEM18] A.J. Dempster *A New Method of Positive Ray Analysis*, Phys. Rev. **11**, 316-325 (1918)

[DEW80] J. Dewar, Proc. Roy. Soc. (London) **36**, 164 (1880)

[DEW88a] J. Dewar, Proc. Roy. Inst. G.B. **12**, 557 (1888)

[DEW88b] J. Dewar, Proc. Roy. Soc. (London) **43**, 1078 (1888)

[DEX53] D.L. Dexter, J. Chem. Phys. **21**, 836-850 (1953)

[DRE94] G.Drechsler, C.Baßmann, U.Boesl, and E.W.Schlag, Z. f. Naturforsch. **49a**, 1256-1258 (1994)

[DRZ84] P.S. Drzaic and J.I. Brauman, J. Am. Chem. Soc. **106**, 3443-3446 (1984)

[EIN05] A. Einstein, *Über einen die Erzeugung und Verwandlung des Lichtes betreffenden heuristischen Gesichtspunkt*, Annalen der Physik **6**, 132-148 (1905)

[ELA84] H.H.D. Eland (Editor), *Photoelectron Spectroscopy*, Butterworths, London (1984)

[ELS63] M.A. El-Sayed, J. Chem. Phys. **38**, 2834-2838 (1963)

[ELS68] M.A. El-Sayed, Acc. Chem. Res. **1**, 8-16 (1968)

[ENG70] R. Englman and J. Jortner, Mol. Phys. **18**, 145-164 (1970)

[ENG76] P.C. Engelking and W.C. Lineberger, J. Chem. Phys. **65**, 4323-4324 (1976)

[EPP97] A.T.J.B. Eppink and D.H. Parker, Rev. Sci. Instrum. **68**, 3477-3485 (1997)

[ERN95] L. Ernster and G. Dallner, *Biochemical, physiological and medical aspects of ubiquinone function.*, Biochim. Biophys. Acta. **1271**, 195-204 (1995)

[EVA57] D.F. Evans, *Perturbation of singlet-triplet transitions of aromatic molecules by oxygen under pressure*, J. Chem. Soc. **257**, 1351-1357 (1957)

[FAN78] H.L.-B. Fang, R.J. Thrash and G.E. Leroi, Chem. Phys. Lett. **57**, 59-63 (1978)

[FER06] G.C. Ferreira, C.C. Schmitt and M.G. Neumann, J. Braz. Chem. Soc. **17**, 905-909 (2006)

[FOE48] T. Förster, Annalen der Physik **437**, 55-75 (1948)

[FU11] Q. Fu, J. Yang and X.-B. Wang, J. Phys. Chem. A **115**, 3201-3207 (2011)

[FUJ89] H. Fujioka, Y. Nishiyama, H. Furukawa and N. Kumada, Antimicrob. Agents Chemother. **33**, 6-9 (1989)

[GAG02] L. Gagliardi, G. Orlandi, V. Molina, P.-Å. Malmqvist and B. Roos, J. Phys. Chem. A **106**, 7355-7361 (2002)

[GAN88a] G. Ganteför, K.H. Meiwes-Broer and H.O. Lutz, Phys. Rev. A **37**, 2716-2718 (1988)

[GAN88b] G. Ganteför, M. Gausa, K.H. Meiwes-Broer and H.O. Lutz, Faraday Discuss. Chem. Soc. **86**, 197-208 (1988)

[GIN01] R. Giniger, T. Hippler, S. Ronen, and O. Cheshnovsky, Rev. Sci. Instrum. **72**, 2543-2550 (2001)

[GRO79] H. Gröner and D. Schulte-Frohlinde, J. Phys. Chem. **83**, 3107-3118 (1979)

[HA83] T.-K. Ha, Mol. Phys. **6**, 1471-17479 (1983)

[HAN92] D. Hanstorp and M. Gustafsson, *Determination of the Electron Affinity of Iodine*, J. Phys. B: Atom. Mol. Opt. Phys.**25** (1992)

[HAN95] H. Handschuh, G. Ganteför and W. Eberhardt, Rev. Sci. Instrum. **66**, 3838-3843 (1995)

[HEC95] A.J.R. Heck and D.W. Chandler, Annu. Rev. Phys. Chem. **46**, 335-372 (1995)

[HEI83] L.A. Heimbrook, B.E. Kohler and T.A. Spiglanin, Proc. Natl. Acad. Sci. USA **80**, 4580-4584 (1983)

[HEI06] B. Heinz, B. Schmidt, C. Root, H. Satzger, F. Milota, B. Fierz, T. Kiefhaber, W. Zinth and P. Gilch, Phys. Chem. Chem. Phys. **8**, 3432-3439 (2006)

[HER33] G. Herzberg and E. Teller, Z. Phys. Chem. **B21**, 410-466 (1933)

[HER75] W.G. Herkstroeter, J. Am. Chem. Soc. **97**, 4161-4167 (1975)

[HEL93] H. Helm, N. Bjerre, M.J. Dyer, D.L. Hueststis and M. Saeed, Phys. Rev. Lett. **70**, 3221-3224 (1993)

[HIL96] E.F. Hilinski, W.M. McGowan, D.F. Sears Jr. and J. Saltiel, J Phys. Chem. **100**, 3308-3311 (1996)

[IKE85] T. Ikeyama and T. Azumi, J. Phys. Chem. **89**, 5332-5333 (1985)

[IKE94] T. Ikeyama and T. Azumi, J. Phys. Chem. **98**, 2832-2835 (1994)

[ITO87] T. Itoh and B.E. Kohler, J Phys. Chem. **91**, 1760-1764 (1987)

[ITO95] T. Itoh, Chem. Rev. **95**, 2351-2368 (1995)

[ITO07] T. Itoh, J Phys. Chem. A**111**, 3502-3506 (2007)

[JAB35] A. Jablonski, Z. Physik **94**, 38-46 (1935)

[KAS50] M. Kasha, Discuss. Faraday Soc. **9**, 14-19 (1950)

[KEL09] J.X. Kelly, M.J. Smilkstein, R. Brun, S. Wittlin, R.A. Cooper, K.D. Lane, A. Janowsky, R.A. Johnson, R.A. Dodean, R. Winter, D.J. Hinrichs, M.K. Riscoe, Nature **459**, 270-273 (2009)

[KEN92] K.M. Ervin and W.C. Lineberger, *Photoelectron spectroscopy of molecular anions*, Adv. Gas Phase Ion Chem. **1**, 121-166 (1992)

[KIN89] G.R. Kinsel and M.V. Johnston, Int. J. Mass Spectrom Ion Processes **91**, 157-176 (1989)

[KIT89] T.N. Kitzopoulus, I.M. Waller, J.G. Loeser and D.M. Neumark, Chem. Phys. Lett. **159**, 300-306 (1989)

[KLA92] D. Klar, M.-W. Ruf and H. Hotop, Chem. Phys. Lett.**189**, 448-454 (1992)

[KLE83] D. Klemp and B. Nickel, Chem. Phys. **78**, 17-28 (1983)

[KLO77] C.E. Klots and R.N. Compton, J. Chem. Phys. **67**, 1779-1800 (1977)

[KNO98] W.J. Knott, J. Schiedt, R. Weinkauf and E.W. Schlag, unpublished results (1998)

[KOH84] B.E. Kohler and T.A. Spiglanin, J. Chem. Phys. **80**, 5465-5471 (1984)

[KOO34] T. Koopmans, Physica **1**, 104-113 (1934)

[KOY70] M. Koyanagi, Y. Kogo and Y. Kanda, J. Mol. Spectrosc. **34**, 450-467 (1970)

[KRU83] P. Kruit and F.H. Read, J. Phys. E. **16**, 313-324 (1983)

[KUE11] B. Küpper, M. Kleinschmidt, K. Schaper and C.M. Marian, Chem. Phys. Chem. **12**, 1872-1879 (2011)

[KUP79] A. Kuppermann, W.M. Flicker and O.A. Mosher, Chem. Rev. **79**, 77-90 (1979)

[LAP25] O. Laporte and W.F. Meggers, *Some rules of spectral structure*, J. Opt. Soc. Am. **11**, 459-460 (1925)

[LEE72] W.H. van Leeuwen, J. Langelaar and J.D.W. van Voorst, Chem. Phys. Lett. **13**, 622-624 (1972)

[LEW44] G.N. Lewis and M. Kasha, J. Am. Chem. Soc. **66**, 2100-2116 (1944)

[LEW45] G.N. Lewis and M. Kasha, J. Am. Chem. Soc. **67**, 994-1003 (1945)

[LIR77] E.C. Lira (Editor), *Excited states, Vol III*, Academic Press, New York (1977)

[LOW66] S.K. Lower and M.A. El-Sayed, Chem. Revs. **66**, 199-241 (1966)

[MAJ84] T.J. Majors, U. Even and J. Jortner, J. Chem. Phys. **81**, 2330-2338 (1984)

[MAM73] B.A. Mamyrin, V.I. Karataev, D.V. Shmikk and V.A. Zagulin, Sov. Phys.-JETP **37**, 45-48 (1973)

[MAR85] J.Marks, P.B. Comita and J.I. Brauman, J. Am. Chem. Soc. **107**, 3718-3719 (1985)

[MAR91a] G. Markovich, R. Giniger, M. Levin and O. Cheshnovsky, J. Chem. Phys. **95**, 9416 (1991)

[MAR91b] G. Markovich, R. Giniger, M. Levin and O. Cheshnovsky, Z. Phys. D: At., Mol. Clusters **20**, 69-72 (1991)

[MAR94] G. Markovich, S. Pollack, R. Giniger and O. Cheshnovsky, J. Chem. Phys. **101**, 9344-9353 (1994)

[MAR11] C.M. Marian, unpublished results (2011)

[MCG69] S.P. McGlynn, T. Azumi, M. Kinoshita, *Molecular Spectroscopy of the Triplet State*, Prentice-Hall, Inc., Englewood Cliffs, New Jersey (1969)

[MIN62] L. Minnhagen, Ark. Fys. **21**, 415-465 (1962)

[MIT00] M. Mitsui and Y. Ohshima, J. Phys. Chem. A **104**, 8638-8648 (2000)

[MIZ09] W. Mizukami, Y. Kurashige, M. Ehara, T. Yanai and T. Itoh, J. Chem. Phys. **131**, 174313/1-10 (2009)

[MOL97] V. Molina, M. Merchán and B.O. Roos, J. Phys. Chem. A **101**, 3478-3487 (1997)

[MUE84a] K. Müller-Dethlefs, M. Sander and E.W. Schlag, Chem. Phys. Lett. **112**, 291-294 (1984)

[MUE84b] K. Müller-Dethlefs, M. Sander and E.W. Schlag, Z. Naturforsch. A **39**, 1089-1091 (1984)

[MUG87] M.L. Muga, Anal. Instrum. **16**, 31-50 (1987)

[NEL05] D.L. Nelson, M.M. Cox, *Lehninger, Priciples of biochemistry, fourth edition* (2005)

[OHS03] Y. Ohshima, T. Fujii, T. Fujita, D. Inaba and M. Baba, J. Phys. Chem. A**107**, 8851-8855 (2003)

[OST04] A. Osterwalderm, M.J. Nee, J. Zhou and D.M. Neumark, J. Chem. Phys. **121**, 6317-6323 (2004)

[PAM99] R. Pou-Amérigo, M. Merchán and E. Orti, J. Chem. Phys. **110**, 9536-9546 (1999)

[PEL09] R.J. Pelaez, C. Blondel, C. Delsart and C. Drag, *Pulsed photodetachment microscopy and the electron affinity of iodine*, J. Phys. B: Atom. Mol. Opt. Phys. **42**, 125001 (2009)

[PLA00] M. Planck, *Zur Theorie des Gesetzes der Energieverteilung im Normalspectrum*, Verhandlungen der Deutschen physikalischen Gesellschaft **17**, 237-245 (1900)

[PER66] H.H. Perkampus, I. Sandeman and C.J. Timmons (Editors), *UV Atlas of Organic Compounds, Vol. 1*, Butterworths, London (1966)

[POW71] H.J. Pownall and J.R. Huber, J. Am. Chem. Soc. **93**, 6429-6436 (1971)

[QUE03] J. Quenneville and T.J. Martinez, J. Phys. Chem. **107**, 829-837 (2003)

[RAI10] V. Rai-Constapel, M. Kleinschmidt, S. Salzmann, L. Serrano-Adrés and C.M. Marian, Phys. Chem. Chem. Phys. **12**, 9320-9327 (2010)

[RAI11a] V. Rai-Constapel, S. Salzmann and C.M. Marian, J. Phys. Chem. A **115**, 8589-8596 (2011)

[RAI11b] V. Rai-Constapel and C.M. Marian, unpublished results, paper in preparation (2011)

[REN34] R. Renner, Z. Phys. **92**, 172-193 (1934)

[REN69] P.M. Rentzepis, Chem. Phys. Lett. **3**, 717-720 (1969)

[REN70] P.M. Rentzepis, Science **169**, 239-247 (1970)

[SAL94] J. Saltiel, D.-H. Ko and S. A. Freming, J. Am. Chem. Soc. **116**, 4099-4100 (1994)

[SAL98] J. Saltiel, S. Wang, D.-H. Ko and D.A. Gormin, J. Phys. Chem. A **102**, 5383-5392 (1998)

[SAL00] J. Saltiel, S. Wang, L. P. Watkins and D.-H. Ko, J. Phys. Chem. A **104**, 11443-11450 (2000)

[SCA80] J.C. Scaiano, J. Am. Chem. Soc. **102**, 7747-7753 (1980)

[SCH97] J. Schiedt and R. Weinkauf, Chem. Phys. Lett. **266**, 201-205 (1997)

[SCH98] J. Schiedt, Ph.D. Thesis, *Photodetachment-Photoelektronenspektroskopie: Erste Schritte zu größeren Systemen*, Technische Universität München (1998)

[SCH99] J. Schiedt and R. Weinkauf, J. Chem. Phys. **110**, 304-315 (1999)

[SCH99b] J. Schiedt and R. Weinkauf, Rev. Sci. Instrum. **70**, 2277-2281 (1999)

[SCH00] J. Schiedt, W.J. Knott, K. Le Barbu, E.W. Schlag and R. Weinkauf, J. Chem. Phys. **113**, 9470-9478 (2000)

[SEM09] Y. Semba, K. Yoshida, S. Kasahara, C.-K. Ni, Y.-C. Hsu, S.H. Lin, Y. Ohshima and M. Baba, J. Chem. Phys. **131**, 24303/1-24303/6 (2009)

[SHE83] J.F. Shepanski, B.W. Keelan and A.H. Zewail, Chem. Phys. Lett. **103**, 914 (1983)

[SHP63a] E.V. Shpol'skii, Usp. Fiz. Nauk **80**, 255-279 (1963)

[SHP63b] E.V. Shpol'skii, Soviet Phys. Usp. **6**, 411-427 (1963)

[SIE10] S. Siegert, Ph.D. Thesis, *Anionen-Photodetachment-Photoelektronen-Spektroskopie als neuer, systematischer Zugang zu dunklen, angeregten Neutralzuständen*, Heinrich-Heine-Universität Düsseldorf (2010)

[SMA77] R.E. Smalley, L.W. Wharton and D.H. Levi, Acc. Chem. Res. **10**, 139-145 (1977)

[STE46] W.E. Stephens, Phys. Rev., **69**, 691 (1946)

[SUG81] K. Suga and M. Kinoshita, Bull. Chem. Soc. Jpn. **54**, 1651-1657 (1981)

[SUZ87] T. Suzuki and M. Ito, J. Phys. Chem. **91**, 3537-3542 (1987)

[SV11a] S. Siegert[1], F. Vogeler[1] and R. Weinkauf, Z. Phys. Chem. **225**, 507-516 (2011)

[SV11b] S. Siegert[1], F. Vogeler[1], C.M. Marian and R. Weinkauf, Phys. Chem. Chem. Phys. **13**, 10350-10363 (2011)

[SWE07] P. Schmidt-Weber, Ph.D. Thesis, *Functionalisation of Surfaces: Isomerisation and Chirality of Adsorbed Molecules*, Freie Universität Berlin (2007)

[SYA82] J.A. Syage, W.R. Lambert, P.M. Felker, A.H. Zewail and R.M. Hochstrasser, Chem. Phys. Lett. **88**, 266-270 (1982)

[TAK74] C. Takahashi and S. Maeda, Chem. Phys. Lett. **28**, 22-26 (1974)

[TEK94] Y. Teki, J.U. von Schütz, H. Wachtel, V. Weiss,and H.C. Wolf, *Triplet excitations in diphenylbutadiene and diphenylhexatriene single crystals by zero-field delayed fluorescence ODMR*, Chem. Phys. Lett. **225**, 124-130 (1994)

[TEL37] H.A. Jahn, E. Teller, *Stability of Polyatomic Molecules in Degenerate Electronic States. I. Orbital Degeneracy*, Proc. R. Soc. Lond. A **161**, 220-235 (1937)

---

[1] These co-workers contributed equally to this work

[TER43] A. Terenin, Acta. Physicochim. U.R.S.S. **18**, 210-241 (1943)

[TER44] A. Terenin, Zhur. Fiz. Khim. **18**, 1-6 (1944)

[THO13] J.J. Thomson, *Rays of positive electricity*, Proceeding of the Royal Society A. **89**, 1-20 (1913)

[THO97] J.J. Thomson, *Cathode Rays*,Philosophical Magazine Series 5. **44**, 293-316 (1897)

[THO79] G. Ter Horst and J. Kommandeur, Chem. Phys. **44**, 287-293 (1979)

[TSC06a] M. Tschurl and U. Boesl, Int. J. Mass. Spectrom. **249-250**, 364-369 (2006)

[TSC06b] M. Tschurl, U. Boesl and S. Gilb, J. Chem. Phys. **125**, 194310-194310/7 (2006)

[TSC07] M. Tschurl, Christoph Ueberfluss and U. Boesl, Chem. Phys. Lett. **439**, 23-28 (2007)

[TUR70] D.W. Turner, *Molecular Photoelectron Spectroscopy*, John Wiley and Sons, London (1970)

[VEE73] H. Veenvliet and D.A. Wiersma, Chem. Phys. Lett. **22**, 87-90 (1973)

[VIS56] G. Viswanath and M. Kasha, J. Chem. Phys. **24**,574-577 (1956)

[VOE95] D. Voet and J.G. Voet (Editors), *Biochemistry*, John Wiley and sons, New York, chapt. 22 (1995)

[VOG09] F. Vogeler, Diploma Thesis, *Effiziente, gepulste Erzeugung von Anion aus Chromophoren mit biologischer Relevanz*, Heinrich-Heine-Universität Düsseldorf (2009)

[VS11] F. Vogeler[2], S. Siegert[2], C.M. Marian and R. Weinkauf, Chem. Phys. Chem. **12**, 1948-1956 (2011)

[WAN99] L.S. Wang, C.F. Ding, X.B. Wang and S.E. Barlow, Rev. Sci. Instrum. **70**, 1957-1966 (1999)

[WEB01] J. Weber, K. Malsch and G. Hohlneicher, Chem. Phys. **264**, 275-318 (2001)

[WEI89] R. Weinkauf, K. Walter, C. Weickhardt, U. Boesl and E.W. Schlag, Z. Naturforsch. **44a**, 1219-1225 (1989)

[WEI92] V. Weiss, H. Port, and H.C. Wolf, *Direct optical detection of the triplet T_1-state in diphenylpolyene single crystals*, Chem. Phys. Lett. **192**, 289-293 (1992)

[WEI10] A. Weigel and N.P. Ernsting, J. Phys. Chem. B **114**, 7879-7893 (2010)

[WIL55] W.C. Wiley and I.H. McLaren, Rev. Sci. Instrum. **26**, 1150-1158 (1955)

[WOO75] M.H. Wood, Theor. Chim. Acta **36**, 345-349 (1975)

---

[2] These co-workers contributed equally to this work

A. Publications

Some of the results of this work are presented in the following publications:

S. Siegert, F. Vogeler, J. Schiedt and R. Weinkauf, *Direct spectroscopy of contact charge transfer states: Possible consequences for tryptophan excited-state deactivation pathways by O_2 and formation of reactive oxygen species*, Phys. Chem. Chem. Phys. **12**, 4996-5006 (2010)

S. Siegert[1], F. Vogeler[1] and R. Weinkauf, *Direct access to the dipole-forbidden $n\pi^*$ T_1 state of p-benzoquinone by photodetachment photoelectron spectroscopy*, Z. Phys. Chem.**225**, 507-516 (2011)

S. Siegert[1], F. Vogeler[1], C.M. Marian and R. Weinkauf, *Throwing light on dark states of a-oligothiophenes of chain lengths 2 to 6: radical anion photoelectron spectroscopy and excited-state theory*, Phys. Chem. Chem. Phys. **13**, 10350-10363 (2011)

F. Vogeler[1], S. Siegert[1], C.M. Marian and R. Weinkauf, *T_1, T_2 state energies and electron affinities of small α,ω-diphenylpolyenes investigated by anion photodetachment photoelectron spectroscopy and excited-state theory*, Chem. Phys. Chem. **12**, 1948-1956 (2011)

---

[1] These co-workers contributed equally to this work

B. List of abbreviations

AC Acridone
AO Atom orbital
CT Charge-transfer
DFT Density functional theory
DPB *all-trans*-1,4-Diphenyl-1,3-butadiene
DPH *all-trans*-1,6-Diphenyl-1,3,5-hexatriene
EA Electron affinity
EEL Electron energy loss
EELS Electron energy loss spectroscopy
EPA Mixed ether, pentane and alcohol solvent
ESI Electrospray ionization
ETC Electron transport chain
eV Electron volts
HOMO Highest occupied molecular orbital
IE Ionization energy
IC Internal conversion
ISC Intersystem crossing
IVR Internal vibrational redistribution
LASER Light amplification by stimulated emission of radiation
LHC Light-harvesting complexes
LUMO Lowest unoccupied molecular orbital
MCA Multichannel analyzer
MCP Microchannel plate
MO Molecular orbital
MRCI Multi-reference configuration interaction
MS Mass spectrometry
Nd:YAG Neodymium-doped yttrium aluminum garnet

ODMR Optically detected magnetic resonance

OPO Optical parametric oscillator

OPOE One-photon-one-electron principle

pBQ p-Benzoquinone

PD Photo detachment

PD-PES photo detachment photo electron spectroscopy/spectrum

PES Photo electron spectroscopy

RF Radio frequency

SB *trans*-Stilbene

SCSHC Sum of the squared contributions of single-hole configurations

SEM Secondary emission electron multiplier

SEVI Slow electron velocity-map imaging

SNR Signal-to-noise-ratio

SOC Spin-orbit coupling

TX Thioxanthone

TOF Time-of-flight

TOF-MS Time-of-flight mass spectrometry

UV Ultra-violet

VIS Visible

VMI Velocity-map imaging

XA Xanthone

ZEKE Zero kinetic energy electrons

C. List of Figures

D. List of Tables